MULTI-SCALE CHARACTERIZATION OF BIOMATERIALS USING COMPLEMENTARY X-RAY AND ELECTRON IMAGING TECHNIQUES

By JAMES TEDSCO, B.M.SC., B.ENG.

A Thesis Submitted to the School of Graduate Studies in Partial Fulfilment of the Requirements for the Degree Master of Applied Science

MASTER OF APPLIED SCIENCE (2017)

Materials Science and Engineering

McMaster University, Hamilton, Ontario, Canada

TITLE: Multi-scale characterization of biomaterials using complementary x-ray and electron imaging techniques

AUTHOR: James Tedesco, B.M.Sc. (Western University), B.Eng. (McMaster University)

SUPERVISOR: Professor Kathryn Grandfield

NUMBER OF PAGES: xiii, 56

LAY ABSTRACT

The continued development of next generation biomedical materials, otherwise known as biomaterials, is in part dependant on the resources and technology that exist to drive manufacturing, characterization, and testing. Biomaterials are being designed and controlled at length scales smaller than the diameter of a single hair, and therefore specialized tools are required to accurately investigate and characterize these new designs. Two such tools are X-ray and electron microscopy, which can be used to image and understand three-dimensional biomaterials non-destructively, and with high resolution, respectively. However, both imaging techniques struggle to provide both. This thesis aims to develop and apply a complementary workflow using X-ray and electron microscopy to investigate two diverse biomaterials: a titanium dental implant, and collagen tissue scaffold, with high resolution, and in three dimensions.

ABSTRACT

Biomaterials may be any class of material that aids in the regeneration, replacement, or augmentation of damaged tissues. The design of biomaterials is becoming increasingly sophisticated as new technologies enable the manufacture and incorporation of smaller components and structural features. Thus, a demand for equally sophisticated tools and methods to study biomaterials are necessary. Two such tools are X-ray micro-computed tomography (micro-CT) and electron microscopy. Micro-CT has the advantage of imaging materials in 3D and non-destructively, but cannot reach the same resolving power as electron microscopy. However, electron microscopy has limited application with biomaterials due to destructive sample preparation requirements. The advantages and limitations of each imaging technique presents a complementary relationship between the two. This thesis aims to develop and apply a complementary workflow using X-ray and electron microscopy to investigate two diverse biomaterials: a titanium dental implant, and collagen tissue scaffold.

In a pilot study, a 3D printed titanium dental implant with a novel dual-stemmed design was investigated for its biocompatibility *in vivo*. Dual-stemmed and conventional conical implants were inserted into the tibia of New Zealand White rabbits for 3 and 12 weeks, then retrieved with surrounding bone. The implants were analyzed using micro-CT, electron microscopy, and histology. Active bone growth and remodelling around the dual-stemmed implant at both time points was observed. Comparative bone-implant contact indicated the dual-stemmed implants supported bone-implant integration, and demonstrates the comparable biocompatibility of these 3D printed stemmed implants in rabbits up to 12 weeks.

In a separate study, a gold functionalized collagen scaffold for tissue engineering applications has been developed. This scaffold design is intended for improved detection of scaffold degradation behaviour *in vivo* using X-ray CT. In this thesis, micro-CT and electron microscopy were used to analyze the resultant scaffold structure after fabrication, as it is important for understanding the outcomes of *in vivo* experiments. Imaging revealed a highly heterogeneous structure at both the micron and nanometer length scales. Interconnected pores from 50 – 400 μm made up 80% of the scaffold volume, while gold nanoparticles and agglomerates ranging from 16 – 1000 nm were non-uniformly dispersed at the nanoscale throughout the collagen matrix.

This work highlights how complementary X-ray and electron microscopy can be applied to characterize diverse biomaterials during developmental and pre-clinical phases.

ACKNOWLEDGEMENTS

The search for place and purpose in this increasingly complex world continues to become more difficult, requiring more advanced and refined skills, and pushing the need for higher levels of education. This thesis represents the unison of my two educational backgrounds, medical science and materials engineering, in the field of biomaterials.

To Kathryn Grandfield, whom provided me this great opportunity, I am forever grateful. Throughout all hardships, you pushed me to be the best I could be. You have better prepared me for the next steps of my life, then a decade worth of prior education. Thank you.

To the Grandfield Research Group, past and present, thank you for all your support, both as colleagues and friends. It is important to remember that the bond between people extends farther than just professional interactions. Going to work with friends is much more enjoyable than just going to work. Special thank you(s) go out to Dakota Binkley, Bryan Lee, Dan Osorio, Xiaoyue Wang, and Emily-Rose Creighton for having to put up with me for the longest.

Acknowledgements to all others who have put their finite amount of time into helping me through my Master's experience. This includes the invaluable support of the wonderful staff in the Department of Materials Science and Engineering; Danielle Mather, Jane Mah, Chelsea Gregory, Hannah Abrams, Doug Culley, and Xioagang Li. In addition, to all those at the Health Sciences Electron Microscopy Facility (especially Marcia Reid), the Canadian Center for Electron Microscopy, and McMaster Automotive Resource Centre, thank you for your support and guidance.

Lastly, I am thankful for the encouragement provided to me by my family and friends. Mom and dad, you have always supported me through anything I've wanted to do, no matter how ridiculous it may seem, including three degrees worth of education, none of which are a PhD. Thank you so much.

Table of Contents

LIST OF FIGURES

LIST OF TABLES

LIST OF ABREVIATIONS

Back-scattered electron – BSE

Bone-implant contact – BIC

Bright field – BF

Charge-coupled device – CCD

Computed-tomography - CT

Dark field – DF

Direct metal laser sintering – DMLS

Electron beam melting – EBM

Electron tomography – ET

Focused ion beam – FIB

High angle annular dark field – HAADF

Micro-computed tomography – Micro-CT

Nanoparticle – NP

New cortical bone - NCB

Polyethylene glycol – PEG

Poly(methyl methacrylate) – PMMA

Secondary electron – SE

Scanning electron microscopy – SEM

Stemmed implant technology – SIT

Scanning transmission electron microscopy (STEM)

Spectral-computed tomography – Spectral-CT

Three-dimensions – 3D

Total cortical bone - TCB

Transmission electron microscopy – TEM

Two-dimensions – 2D

Volume of interest - VOI

DECLARATION OF ACHIEVEMENT

I hereby declare the following contribution by myself, colleagues, and collaborators to the completion of this thesis:

CHAPTER 1 – All writing and figures (unless otherwise cited) have been produced by the author.

CHAPTER 2 – The contents of this chapter are currently in submission for publication (International Journal of Dentistry, May 2017). Unless specified below, all sample preparation, experiments, data analysis, and presentation was performed by the author. The dual-stemmed implant was designed by Stemmed Implant Technologies Inc. Implant preparation for surgery was performed by Bryan E.J. Lee. Animal housing, surgical procedures, retrieval of specimens, and histology were performed by trained professionals at the Central Animal Facility, McMaster University. Preparation of the TEM specimen by FIB was performed at the Canadian Center for Electron Microscopy. Imaging was in part performed by Alex Lin, Kristoff Malejczuk, and Kathryn Grandfield. Writing was performed in part by Dakota Binkley. Figures were assembled in part by Bryan E.J. Lee.

CHAPTER 3 – Unless specified, all sample preparation, experiments, data analysis, and presentation was performed by the author. Specimens were designed and produced at the University of Notre Dame in the lab of Dr. Ryan Roeder. TEM samples were prepared at the Electron Microscopy Facility, Faculty of Health Sciences, McMaster University. Electron tomography was performed with assistance at the Canadian Centre for Electron Microscopy. Data analysis was performed in part by Iflah Shahid.

CHAPTER 4 – All writing was produced by the author.

CHAPTER 1: INTRODUCTION

Development of Biomaterials

Biomaterials are a material class intended to improve health and wellbeing. The innovation, development and commercialization of biomedical devices is a relatively new occurrence, however, the use of materials for medical applications predates modern civilization [1]–[3]. Until Dr. Joseph Lister developed the aseptic surgical technique in the 1860s, implant biomaterials were largely unsuccessful due to infection [4]. Afterwards, much attention was put into optimizing the mechanical properties of biomaterials, commonly used for repairing long bones and joints [5], however most implant biomaterials still had a low probability of success due to a poor understanding of biocompatibility. It was the advent of World War II that pushed the development of the first generation of modern biomaterials we know today [6]–[8]. This was due to the availability of high performance materials, previously meant for combat, and the observation of how these materials reacted in soldier's injuries. The use of polymers as biomaterials for cardiovascular surgery began, and an understanding of biocompatibility was developed. At this time, biocompatibility was viewed as a biological inertness, such that the biomaterial caused little to no immune response and toxicity [7], [8].

It wasn't until the 1980s at two independent consensus conferences, one American and one European, that definitions of a *biomaterial* were debated and derived. Both definitions are widely cited. At the Consensus Development Conference on the Clinical Applications of Biomaterials held at the National Institutes of Health (Mayland, USA) in 1982, a biomaterial was defined as, "any substance (other than a drug) or combination of substances, synthetic or natural in origin, which can be used for any period of time, as a whole or as a part of a system which treats, augments, or replaces any tissue, organ, or function of the body" [9]. While at the Consensus Conference on Definitions in Biomaterials Science, in 1987, of the European Society for Biomaterials, a biomaterial was defined as 'a non-viable material used in a medical device, intended to interact with biological systems' [10]. This definition was debated and revised in 1999, as 'a material intended to interface with biological systems to evaluate, treat, augment or replace any tissue, organ or function of the body' [11]. The term *biocompatibility* was also defined as, 'the ability of a material to perform with an appropriate host response in a specific application' [11]. This definition has two important aspects. First, the biomaterial must induce a desired biological response with minimal adverse effects (i.e. inflammation or cytotoxicity). Second, the biomaterial must perform it's intended function for the specific application.

While still fundamentally important, a shift from achieving bioinert tissue responses to developing materials that were bioactive and biodegradable occurred from the 1970s – 2000 [8]. The ability of biomaterials to elicit specific and controlled interactions with the surrounding tissue, and to break down in a manner that allows regenerating tissue to replace the foreign material, significantly increased the clinical applications of biomaterials. As opposed to the biomaterials that were developed in the late 20th century, which were generally either bioactive or biodegradable, the biomaterials of the 21st century are usually designed to achieve both characteristics. In this way, todays biomaterials are created to aid in the regeneration, and not simply replacement, of injured tissues, giving way to the era of *tissue*

engineering. Tissue engineering utilizes a combination of biomaterials (commonly as a scaffold), cells, and cell signaling molecules to create three-dimensional (3D) tissues and organs [12]. The biomaterial scaffold is a porous structure which acts to; provide an initial support for cellular placement, induce cellular migration, and facilitate tissue growth and organization. Scaffolds are usually natural or synthetic polymers that can be constructed in a variety of forms, including; sheets, gels, and highly complex 3D structures with detailed pores and channels [13]–[16]. Polymers are generally better scaffold materials because they tend to be more ductile, formable, and biodegradable than metals. While polymers are the most common material for tissue engineering applications, metallic implant biomaterials remain the material of choice for load bearing applications, such as artificial hip joints, bone plates, and dental implants, because they are very reliable mechanically [17], [18].

Motivation and Aims

As the structural complexity of biomaterials increases, it is important to develop and use tools that can facilitate the characterization of these biomaterials. Microscopy is one such fundamental tool used to characterize and understand the structure and function of many, if not all, engineered devices, including biomaterials. Advances in microscopy such as improved resolving power, and 3D and non-destructive techniques have paralleled and facilitated the advancement of biomaterial engineering, however, challenges still exist. Current challenges for imaging biomaterials include:

- Biomaterials vary greatly in their material makeup, as they can be made of metallic, ceramic, or polymeric materials, or occur in any combination of these, making the selection of optimal imaging conditions difficult.
- Biomaterials are applied in sensitive biological settings, creating complex imaging environments that are prone to damage and artifacts.
- It is important to characterize biomaterials across multiple length scales, as these features can facilitate important functions, while maintaining a representable volume assessment (sampling size) in 3D. A trade off exists in microscopy between increasing resolution and magnification, and decreasing the sampling size.
- *In vivo* studies of biomaterials typically involve invasive procedures that remove the biomaterial from the model for imaging and assessment. This has ethical implications and causes variability in the data.

No single imaging technique exists that can meet all these challenges. The current method is to use multiple complementary imaging techniques, specific to the goals of biomaterial study, which together attempt to provide all necessary information.

This thesis aims to **develop and apply a complementary workflow** using **X-ray** and **electron microscopy** to investigate two diverse biomaterials: a **titanium dental implant** and **collagen tissue scaffold**, to understand their structure and function as biomaterials. The thesis is organized such that background information on imaging is provided, followed by background pertinent to each biomaterial study within their respective chapters.

Complementary Imaging Techniques

To evaluate biomaterial outcomes, visualization and monitoring of biomaterial/scaffold structure and biocompatibility are essential. It is ideal to perform such imaging in a non-destructive and non-invasive fashion, with high magnification and resolution, requiring specialized imaging techniques [19]. Many imaging tools exist, and all forms involve the interaction of electromagnetic or mechanical energy (waves) with an object. Absorption, refraction, or scatter interactions are detected, quantified, and displayed to create an image. The imaging depth, contrast, and spatial resolution (resolving power) achieved by a given imaging modality are dependent on the type and wavelength of energy employed, and the physics of the imaging system. The imaging depth can be important for biomedical applications as non-invasive imaging is necessary in clinical settings [20]. No single imaging technique can provide all desired imaging properties [19]. Magnetic resonance, nuclear, X-ray and ultrasound imaging are commonly used in diagnostic medicine due to their non-invasive capabilities, while optical and electron microscopy are employed to assess extracted biomaterials due ease of use and high resolution, respectively.

Here X-ray and electron microscopy are described. Table 1 compares important imaging properties between the two.

Table 1. Comparison of imaging media used in micro-CT and electron microscopy

	Micro-Computed Tomography	**Electron Microscopy**
Imaging medium	X-rays	Electrons
Wavelength (nm)	0.01 – 10	0.002 – 0.012
Resolution (nm)	1000 – 5000	0.05 – 5
Penetration Depth	Centimeters	Nanometers
Non-Destructive	Yes	No
Three-Dimensional	Yes	No

X-ray Micro-Computed Tomography

Micro-computed tomography (micro-CT) is a non-destructive imaging technique that uses X-ray–material interactions to produce images of the material in 3D, and with micron resolution. *Computed tomography* creates images of objects as a series of cross sectional slices, known as orthoslices, over its entire volume, synonymous to the stacking of bread slices to reform the loaf. The process works by *acquiring* many X-ray projection images around the object over 180˚ or 360˚, and *reconstructing* the projections into orthoslices using computed mathematical algorithms.

The principal components of a micro-CT scanner are illustrated in Figure 1. An X-ray beam is generated and directed toward a specimen. Only a portion of the incident X-ray photons will pass through the specimen and be detected. By detecting the number and location of X-ray photons which traversed the specimen a projection image can be formed. To interpret and analyse the resultant images it is important to understand the underlying X-ray–material interactions.

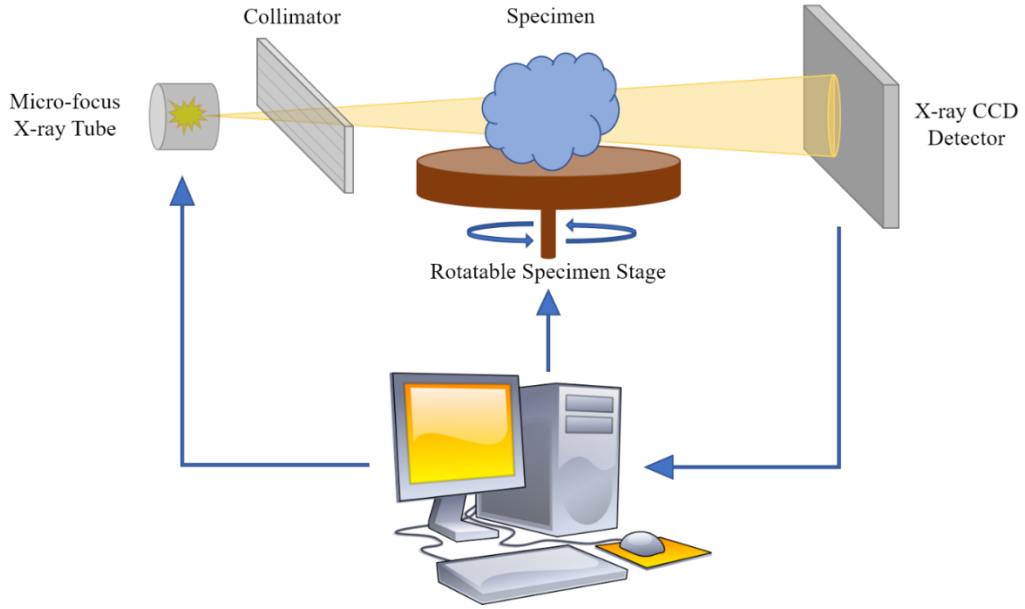

Figure 1. Principal components of a micro-CT scanner. A micro-focus X-ray tube produces radiation, which is collimated and passed through the object. The radiation is attenuated by the sample, and this attenuation is measured and displayed by a CCD camera with a phospholayer coating to convert X-rays to visible light. The entire process is controlled by a computer.

X-ray Interactions with Matter and Attenuation

X-rays are a form of electromagnetic radiation existing as photons within a specific range of energy of the electromagnetic spectrum. They are short wavelength (0.01nm– 10 nm), high energy (124eV – 124 keV) waves. X-rays can be further divided into hard and soft X-rays, where hard X-rays are higher energy (12.4 – 124 keV) and soft X-rays are lower energy (124 eV – 12.4 keV). Due to the penetrating ability of hard X-rays (high energy) they are used to image the inside of objects non-destructively.

As the X-ray beam passes through a specimen, these X-ray photons interact with the specimen material, attenuating (impeding) their propagation. X-ray attenuation is the reduction in the intensity of an X-ray beam as it traverses matter. The attenuation of X-ray intensity by an object is dependant on four factors; (1) X-ray beam energy, and the attenuating material's, (2) composition, (3) density, and (4) thickness. Individual X-ray attenuation events (X-ray–material interactions) depend on the X-ray beam energy and material composition, whereas the total extent of attenuation depends on the number of these X-ray–material interactions, which depends on the material's density, and thickness. There are two important X-ray–material interaction events that occur within the X-ray energy range used for imaging: photoelectric absorption and Compton scattering.

Photoelectric Absorption – A photoelectric interaction between an X-ray photon and material atom causes absorption of the X-ray photon. Photoelectric absorption prevails in high atomic number (Z) materials and low energy (Figure 2).

Compton Scattering – An inelastic interaction between an X-ray photon and material atom causes the photon to lose kinetic energy and scatter. The probability of Compton scattering is independent of atomic number, meaning the scattered X-rays contain little contrast between materials. Compton scattering dominates X-ray attenuation for low atomic (Z) materials and high energy photons (Figure 2).

X-ray images depend on differences in atomic number to produce sufficient contrast to differentiate anatomic structures. Absorption interactions produce good contrast, while scattering interactions decrease contrast and increase image noise. Imaging of biological tissues and polymer biomaterials is limited because they are comprised of low Z elements where Compton scattering dominates attenuation [21]. Metallic biomaterials tend to have photoelectric interactions within the X-ray imaging energy range and the resultant images have improved contrast [22].

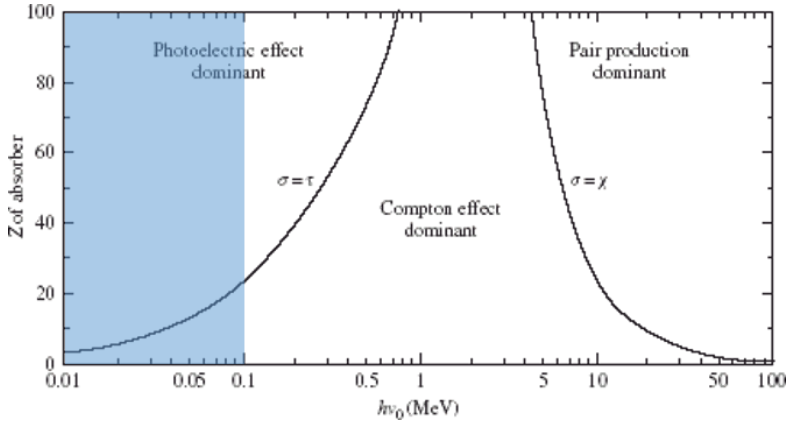

Figure 2. Attenuation domains for the competing X-ray interactions, adapted from Cooper et al. (2004). The lines indicate where the interactions are equal for a particular Z element and photon energy. The blue region indicates the energies used for X-ray imaging.

Biomaterial Imaging Using Micro-Computed Tomography

The non-destructive nature of X-ray CT makes it a very attractive tool to image materials in an unaltered state. However, early use of X-ray CT was limited because of poor contrast of low Z materials, such as, most biological tissues and polymeric materials, and insufficient resolving power. However, due to technological improvements of the CT scanner [23], and the use of contrast agents [21], resolution and contrast limitations, respectively, are less cumbersome today, such that many materials, including biomaterials, are now investigated non-destructively, and in 3D using micro-CT. A brief demonstration of how micro-CT has been used to investigate the biomaterial types studied in this thesis will be discussed.

Load Bearing Implants

Micro-CT is a popular technique to study bone-implant interactions of load bearing implants. Integration of metallic implants to bone (osseointegration) followed by appropriate mechanical and biological responses is important in orthopedics and dentistry. Bone is the most visualized tissue using X-rays owing to its relatively high density and calcium

composition, so the non-destructive study of bone-implant interactions with micro-CT is a very useful approach.

Micro-CT has been used to investigate bone volume and bone-implant contact (BIC) reactions to dental implants [24], [25], bone responses and wear deformation of joint (hip, knee, etc.) implants [26]–[28], and bone repair of fixation implants for fracture [29], [30]. The mechanical strength of all load bearing implants is of great importance, such that metals remain the material of choice for these applications, however, they are not all equal with respect to toxicity and bone-implant interactions, and micro-CT has been used to show differences in the biocompatibility of different implant materials [31], [32]. Additionally, with the development of metallic 3D printing techniques, more complex implant geometries are being designed. A current trend is to make porous metallic implants to facilitate improved bone ingrowth and integration, and again, micro-CT has been particularly useful in determining the 3D bone ingrowth within these porous implants [33]–[35].

A disadvantage of using micro-CT to study bone-implant interactions is the occurrence of beam hardening artifacts. Beam hardening occurs because of the polychromatic nature of the X-ray beam, which can appear as cupping or streaking artifacts [36]. This can be particularly problematic when imaging highly attenuating materials such as metals, which act as filters, resulting in darks streaks. It has been shown that even light metals such as titanium cause beam hardening [37]. When analyzing bone-implant interfaces, beam hardening prevents reliable discrimination of bone close to the implant [38]. Methods to reduce beam hardening effects include: pre-specimen filtration of low energy X-rays [39], monochromatic source for X-ray generation [40], and numerical correction algorithms during reconstruction [41].

Tissue Engineering Scaffolds

Just as porosity of load bearing implants is important for bone ingrowth and osseointegration, porosity of tissue engineering scaffolds is even more crucial for successful cell migration, and tissue ingrowth and regeneration. It is important to understand the porosity and interconnectivity of porous scaffolds to predict outcomes, and micro-CT has been used to characterize scaffold porosity in 3D [42]–[44].

A disadvantage of using micro-CT to study scaffolds is the lack of contrast generated by X-rays with low Z materials [21]. Tissue engineering scaffolds are commonly made of polymeric biomaterials due to advantageous properties of many polymers, such as biodegradability and formability [45], however the elemental composition of such materials reduces the achievable contrast in micro-CT images [46]. The use of heavy elements as contrast agents improve the achieved contrast of biological tissues and soft biomaterials [47]. Examples of contrast agents used to image scaffolds with micro-CT include: gold and gadolinium nanoparticles (NPs) for *in vivo* study of PEG and PMMA scaffolds, respectively [48], [49], and osmium tetroxide and uranyl acetate for *in vitro* study of collagen scaffolds [50].

Although the resolution of micro-CT is sufficient to understand overall bone-implant interactions and micro-porosity, this resolving power is not sufficient in characterizing nano-structures. Therefore, it is sometimes necessary to use a technique that has higher resolving power, such as electron microscopy.

Electron Microscopy

Two kinds of electron microscopy are used to image biomaterials and tissues: the transmission electron microscope (TEM) and the scanning electron microscope (SEM). Both work on the same fundamental principle; interactions between an incident electron beam and an object are used to generate an image [51]. Although electrons are not a type of radiation within the electromagnetic spectrum, they exhibit a wave nature, and interact with matter similarly [52]. The benefit of electrons is their extremely small wavelength (Table 1). According to the Reyleigh criterion, the ability to resolve two points in an image is dependant on the imaging radiation's wavelength [52]. In practice, EM can achieve resolutions between 0.05–5 nm depending on the type of electron microscopy [52]. Electron microscopy is a pivotal tool to understand the nanoscale structure of biomaterials.

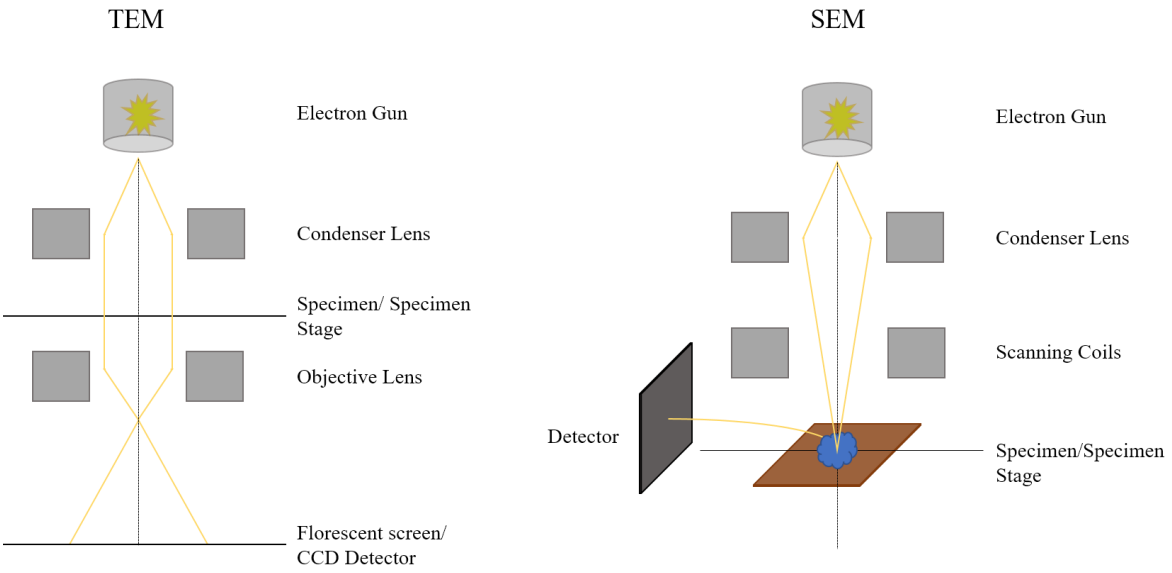

Figure 3. Principal components of TEM and SEM. An electron gun produces a beam of electrons which is accelerated down the optical axis and focused using condenser lenses. The focused beam interacts with the specimen and the signals generated are detected and displayed.

TEM and SEM involve the acceleration of an electron beam towards a specimen, and the detection of specific electron–material interactions. This requires: an electron gun to produce and accelerate electrons, condenser lenses to focus the electron beam on a specimen, a specimen stage, and a signal detection and display system (Figure 3). Key differences between a TEM and SEM are summarized in Table 2. As the name implies, TEM involves the transmission of the incident electron beam, and therefore TEM specimens must be thin enough to be electron transparent (~100 nm) [52]. SEM is a surface imaging technique, and as such, the bulk specimen can be used [51]. TEMs use a parallel beam geometry which illuminates a large portion of the specimen (i.e. floods the specimen), while SEMs uses a convergent beam geometry, creating a small probe which is scanned (rastered) over the specimen [51]. However, certain TEMs can perform probe illumination with a scanned convergent beam, called *scanning transmission electron microscopy* (STEM) [52]. Also, the

electron beam transmitting through the specimen in TEM is collected, magnified and projected using lenses. SEMs do not have post specimen optics, and magnification is a result of the ratio between the raster and display dimensions. To interpret and analyse the EM images, it is important to understand the underlying electron–material interactions.

Table 2. Comparison of a transmission and scanning electron microscope.

	TEM	SEM
Sample Shape	Thin (~100 nm)	Bulk
Beam Penetration	Transmission	Surface
Beam Shape	Parallel or convergent	Convergent
Sample Illumination	Flood or scanning	Scanning
Magnification	Objective lens	Raster size

Electron Interactions with Matter

Although electrons are not a form of radiation within the electromagnetic spectrum, their wave nature allows them to behave as such, producing a wide range of ionizing or scattering events (Figure 4A). Due to the high level of interaction they cannot penetrate deep into matter, and can only be used to image thin sections (~100 nm) or the surface of objects. Each type of electron–material interaction provides different information about the specimen, such as, mass-thickness, crystallographic, and elemental information.

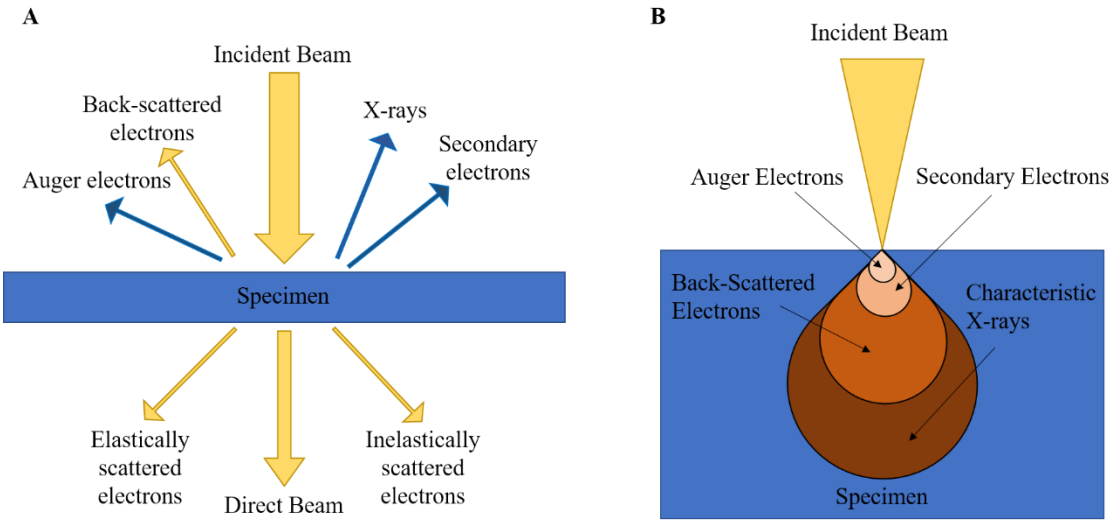

Figure 4. Electron – material interactions. A) Signals generated when a high-energy beam of electrons interacts with a thin specimen. Yellow arrows are incident beam electron signals. Blue arrow are signals emitted from the specimen due to ionizing events. B) Signals generated within the specimen, known as the interaction volume.

Direct Beam – Unimpeded incident electrons that pass through the specimen. These are analogous to the detection of X-rays in micro-CT.

Elastically (forward) Scattered Electrons – As the high energy electron beam passes through the specimen, the electrons are attracted to the specimen atoms (Coulombic interaction). The attraction causes the incident electron to deflect (scatter) without loosening any energy. Coulombic interactions increase with increasing thickness, atomic number (Z) of the respective element, and crystallinity.

Inelastically (forward) Scattered Electrons – As the high energy electron beam passes through the specimen, the incident beam electrons can transfer energy to the atoms of the specimen through a number of interactions. Irrespective of the transfer event, the incident electrons loose energy and are scattered. Inelastically scattered electrons are used to determine the specimen composition because the amount of energy lost by an electron is dependant on the specimen chemical structure.

Back-scattered Electrons (BSEs) – When Coulombic interactions are strong, incident electrons can be scattered at high angles (Rutherford scattering). In some instances, the incident electron is back-scattered (reflected). The probability of a back-scattering event increases with atomic number (Z) of the respective element. BSEs are high energy electrons and therefore have enough energy to come from relatively deep (~1 μm) within the interaction depth (Figure 4B).

Secondary Electrons (SEs) – SEs are ejected electrons from the atoms of the specimen during inelastic interactions (ionizing events) between the electron beam and specimen. They have low energy, and therefore only those originating close to the surface (~100 nm) can escape the specimen (Figure 4B). SEs are useful for imaging the surface morphology of objects.

Auger Electrons – Are SEs ejected from the valence band of the specimen atoms, due to energy transfer from a preceding ionization event. Auger electrons have very low energy, and thus the absorption of these electrons in the specimen occurs readily. Only Auger electrons created close to the surface (<50 nm) can leave the specimen (Figure 4B). The energy of Auger electrons is dependant on the atomic number (Z) of the ejecting atom, and can thus can be used to assess the near surface specimen composition.

All electron–material signals are generated when the electron beam passes through an object. However, only certain individual signals are detected at a given time to form images with useful contrast. Direct beam and elastically scattered electron detection for TEM, and SE and BSE detection for SEM will be briefly described.

Bright Field Imaging

TEM image formation using the *direct beam*, termed **bright field (BF)** imaging, is analogous to X-ray image (radiograph) formation. The intensity of the direct beam is reduced by scattering of the incident beam, which is dependant on the mass-thickness and crystallinity (Bragg diffraction) of the specimen [52]. Contrast is generated as high intensity detection is associated with bright pixels in the image, whereas low intensity (high scattering) detection is associated with dark pixels. In real specimens, mass-thickness and diffraction contrast, occur simultaneously, making the interpretation of BF-TEM images sometimes difficult [52].

Dark Field Imaging

The elastically scattered electrons themselves provide valuable information because they are dependant on the specimen composition and crystallinity. If the direct beam is blocked and the *elastically scattered electrons* are now detected, this is called **dark field (DF)** imaging. The contrast is flipped compared to BF, where bright areas correspond to areas of electron scattering, and dark areas correspond to direct beam transfer. The information provided in DF images is the same as BF (mass-thickness and diffraction contrast), however the reduction in overall intensity (only the scattered portion of the electron beam are detected) tends to improve contrast [52]. Dark field images also suffer from the combined contrast effects of mass-thickness and diffraction, again making interpretation difficult [52].

Interpretation of amorphous materials (i.e. most polymers or biological materials) is usually straight forward because contrast is mainly due to mass-thickness differences [52]. However, when DF imaging crystalline materials it is often desirable to reduce the influence of either mass-thickness or diffraction contrast in images. To reduce mass-thickness effects, a crystalline material can be tilted to a specific crystallographic orientation, enhancing the diffracted contribution of the scattered electrons. To limit diffraction contrast, a specialized mode and detector are used. The detector cannot tell where the detected electrons originate from in the sample, so the sample is imaged point-by-point, by putting the microscope into scanning mode (STEM). The total electron intensity collected at each point (pixel) is proportional to the brightness in the image [52]. The electrons scattered by mass (Z) differences generally occur at higher angles than the electrons scattered by diffraction [52]. By using a high angle annular detector, only the *high angle elastically scattered electrons* are detected, providing compositionally sensitive (Z-contrast) images, otherwise known as **high angle annular dark field (HAADF)** images (Figure 5).

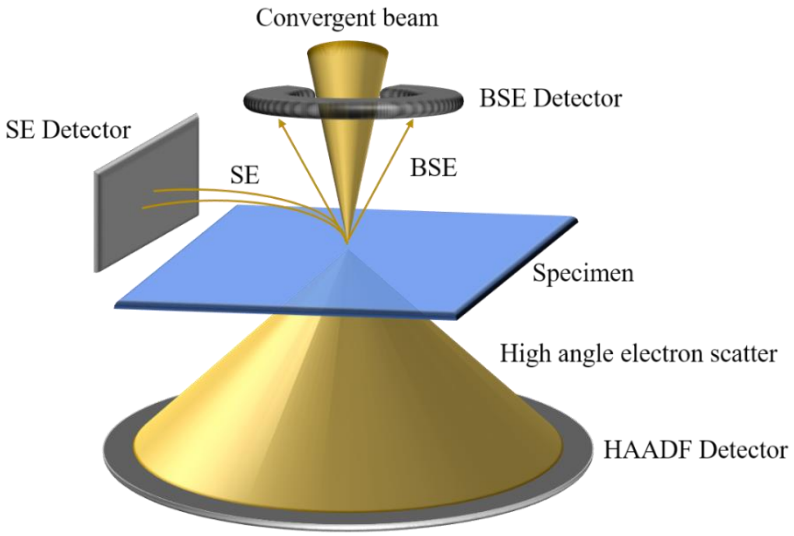

Figure 5. Signal detection for scanning (transmission) electron microscopy–S(T)EM. Secondary electrons and back-scattered electrons are detected in SEM. High angle forward scattered electrons are detected in HAADF-STEM.

The two most commonly used signals for SEM are SEs and BSEs. In the same fashion to STEM, the convergent electron beam is scanned over the specimen and at each point SE and BSE intensities are detected by their respective detectors (Figure 5).

Secondary Electron Imaging

The brightness in a SE image depends on the intensity of SE signal hitting the detector. Useful contrast is generated because convex surfaces allow more SEs to escape than flat and concave surfaces, known as edge effect. Edges appear bright providing a well-defined 3D appearance of the specimen surface, making SE imaging a useful tool to understand the surface structure (topography) of objects.

Back-scattered Electron Imaging

BSEs are reflected beam electrons that escape the interaction volume. Since heavy elements (high atomic number) backscatter electrons more than light elements (low atomic number), heavy atoms appear brighter in the image. BSEs are used to detect contrast between areas with different chemical compositions. It is possible, and common practice, to perform SE and BSE imaging simultaneously.

Biomaterial Imaging Using Electron Microscopy

Electron microscopy is one of the most widely used tools for investigating the structure of biomaterials and their interface to biological tissues. It has been recognized that for the success of biomaterials, knowledge of nanostructures is required. For example, a critical factor for biomaterial integration is the surface topography (e.g. roughness), pore size distribution and interconnectivity, and architecture of included nanofibres and nanoparticles [53]. Owing to its high resolution, EM has the power to resolve such nanostructures in detail. A brief discussion of how EM has been used to investigate the biomaterial types studied in this thesis is discussed.

Load Bearing Implants

The osseointegration of load bearing implants is crucial for their long-term success, and as such, much attention is put into optimizing implant surfaces to facilitate and encourage bone-implant integration. It is well known that increasing surface roughness improves osseointegration [54]–[56], however as bone is a hierarchical material with nano- and micro-organization, the length scale at which implant surface roughness should be controlled is of interest [57]–[59]. Additionally, surface coatings which act to improve the chemical connection of the bone-implant interface are also being researched [60]–[62], and SEM is commonly used to characterize these implant surfaces.

Complementary to micro-CT, SEM is also a popular technique to study the bone-implant interface with load bearing implants [29], [63], [64]. SEM provides improved resolution, so it is better suited to assess the bone-implant interface, however it can only do so for a single exposed surface as compared to the entire volume when micro-CT is used. Nano-sized separations in the interface can be observed using SEM over relatively long implant lengths, giving a better understanding of the BIC. Although, to truly see the bone-implant interface, TEM is needed to resolve such an intimate connection. The nanostructure of the bone-implant interface has been characterized with TEM in 2D and 3D [65]–[67], revealing the structural transition and interconnection of the biological and metallic components.

Tissue Engineering Scaffolds

SEM is frequently used to characterize the micro- and nanostructure of tissue engineering scaffolds. For example, SEM has been used to assess the porosity and surface structure of sintered bioceramic scaffolds suitable for bone tissue engineering applications [13], [68]. While TEM has been used for morphometric analyses of fibre diameter [69], NP size and distribution [70], nanoscale oxide thickness on implant surfaces [71], and ultra-structural analysis of scaffold-cell binding [72].

However, there are disadvantages to EM: a multitude of time consuming and costly processing steps are required, and the possibility of processing artifacts always occurs. For biomaterials and their applications, the technique involves the dehydration and embedding of biological tissues, and cutting (destruction) of the biomaterial to prepare it for imaging, all of which can cause undesired structural alterations. Also, TEM images are limited to 2D projections of the specimen volume, while SEM can provide a 3D interpretation, but of surfaces only. An exception to this is electron tomography (ET), a complex and highly advanced imaging technique.

CHAPTER 2: OSSEOINTEGRATION OF A TITANIUM DENTAL IMPLANT

Motivation and Aims

Bone-anchored implants have been a standard treatment for edentulism (tooth loss) since the mid 1980's after Per-Ingvar Brånemark demonstrated the successful osseointegration of a titanium dental implant placed in human patients [73]. However, failure rates for clinical use dental implants range between 3-8% depending on the implant design and/or patient health factors [74]–[77]. Although this appears to be a rather successful procedure, an epidemiological study reported 1200 emergency department visits due to dental implant failures from 2008-2010 in the US alone [78], signifying the continued burden of edentulism on the healthcare system. As such, methods to improve the clinical outcomes of dental implants are still actively pursued.

Due to its bone-bonding or osseointegrative ability, mechanical and chemical properties, and overall biocompatibility, titanium and titanium alloys have long been the dental implant material of choice [32], [79], [80]. Recently, considerable emphasis has been placed on surface treatment of implants, where surface roughness and texture modifications have been shown to facilitate cellular activity and bone integration via microscale and nanoscale features [57], [81]–[83]. In addition, a range of surface coatings, such as calcium phosphate, magnesium, and titania have been explored with the intent of encouraging faster osseointegration [60], [61], [84]. While it is known that implant geometry can change the response of the bone-implant interface under loading [85], conventional machining processes have traditionally limited implant morphologies to conical and screw-like designs. However, with the technological advances in additive manufacturing, 3D printing of titanium and titanium alloys for new and innovative implant geometries are now possible. Additive manufacturing techniques, such as Direct Metal Laser Sintering (DMLS) and Electron Beam Melting (EBM), are processes that can create 3D metallic constructs by selectively melting metal powder in a layer-by-layer fashion. These techniques are capable of creating complex porous features [16], [86], [87] and an inherent surface roughness, as the melted powder droplets solidify on the object surface. Current use of this technology for implant manufacturing has focused on creating open pore networks to mimic trabecular bone, showing improved cellular activity and greater bone ingrowth in both rabbit and sheep models [35], [88], [89].

This chapter investigates the biocompatibility of a 3D printed dental implant with a novel dual-stemmed shape using complementary histology, X-ray, and electron microscopy. The aims of this study were to:

1. Assess the biocompatibility of the stemmed titanium dental implant.
2. Compare the bone growth and integration of the stemmed titanium dental implant to a stainless steel conventional screw implant.
3. Develop a complementary platform to image the micro to nanoscale bone growth and bone integration.

Background

Bone Structure

Bones support and protect organs, produce red and white blood cells, store minerals, and enable mobility. Bone tissue, or osseous tissue, is the major structural and supportive connective tissue of the body [90]. It is distinct from bones themselves because bones are organs made up of bone tissue, as well as marrow, blood vessels, epithelium and nerves. Bone tissue refers specifically to the mineral matrix that forms the rigid sections of the organ [91]. When classifying bone tissue by structure a hierarchical system is used which is typically divided into macroscale, microscale and nanoscale levels.

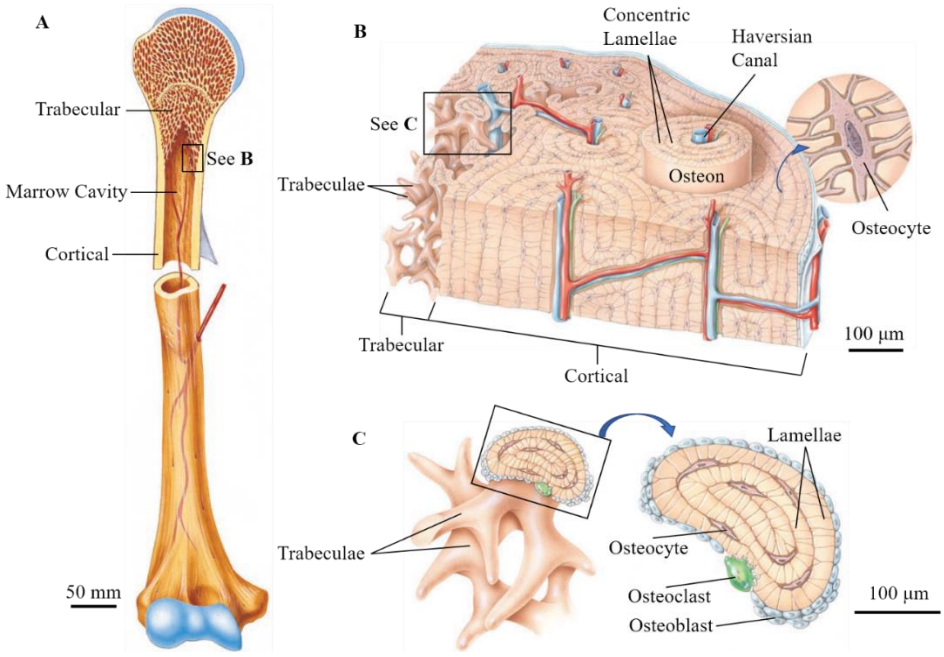

Figure 6. Macroscale and microscale bone structure adapted from [167]. A) Macroscale bone structure of a long bone. Two types of bone tissue exist, cortical and trabecular bone. B) Microscale bone structure reveals the osteon and trabecula. The osteon is comprised of cells (osteocytes), a blood supply (Haversian canal), and bone tissue (concentric lamellae). C) Structure of trabeculae. Semilunar bone lamellae with bone cells (osteocytes, osteoblasts, osteoclasts)

Macroscale

The macroscale structure of bone tissue is divided into *cortical* (compact, dense) and *trabecular* (cancellous, spongey) (Figure 6A). Cortical bone is denser than trabecular bone and forms the hard-outer layer. Trabecular bone is porous, and is mainly found at the ends of bones. The greater porosity and surface area of trabecular bone in comparison with cortical bone makes it more suitable for metabolic activity. The spatial dimensions of cortical and trabecular bone vary greatly between species, bone type, age, gender, and health status [92]–[95]. For example, a human tibia (shin bone) generally has a cortical bone thickness of 8 mm [94], while rabbit tibia has a cortical thickness of about 1 mm [96].

Microscale

At the microscale, cortical and trabecular bone tissues are made of their structural units, osteons and trabeculae, respectively (Figure 6B/C).

Osteons – Osteons of cortical bone are densely packed cylindrical structures consisting of a central Haversian canal (blood vessel) with concentrically arranged lamellae and osteocytes. Osteons can be compared to a stack of logs, each log is made up of rings of hard wood, and together it requires considerable force to fracture them all. It is the lamellar component which provides each osteon its high strength, while the osteocytes form the physiological response system to external stresses. The diameter of an osteon varies far less across species, measuring about 200 μm [97].

Trabeculae – Trabeculae of trabecular bone are irregularly spaced thin columns consisting of semilunar lamellae and osteocytes. The macroscopic spaces between the trabeculae help make bones lighter and are filled with red bone marrow. Similarly to the osteon, the lamellae component of each trabecula provides its strength, while the osteocytes form the physiological response system. Again, the diameter of trabeculae is quite consistent across species, measuring about 100 μm [97].

It is at the microscale where cells are visualized. Three bone specific cells exist which are responsible for the maintenance and turnover of bone tissue.

Osteocytes – Cells within the substance of bone and are involved in cell signaling and maintaining the viability of the bone tissue. They control bone turnover.

Osteoblasts – Cells that lay down bone tissue.

Osteoclasts – Cells that breakdown and resorb bone tissue.

The major difference between cortical and trabecular bone, is not the make up of their structural units, but their overall spacing and packing. It is at the nanoscale which the fundamental structure of bone is revealed.

Nanoscale

Bone lamellae is a composite material comprised of nanoscale organic and inorganic components (Figure 7). *Collagen*, a soft polymer, makes up the organic component, whereas calcium phosphate, a hard *mineral* (usually in the form of hydroxyapatite), makes up the inorganic part. The mineral is responsible for giving bone its hardness, while the collagen is elastic, making the overall bone mechanics tougher. The collagen assumes the form of fibrils which are aligned in the same direction within each lamella, while the exact orientation and position of the mineral with respect to the collagen is still debated.

Collagen fibrils are long cylindrical structures assembled from collagen *molecules*, occurring in a characteristic periodic fashion. The molecules themselves have a 1.5 nm diameter and are 300 nm length [98]. The periodic nature of collagen fibrils is well observed in the TEM, and is typically modelled as repeating units of 5 laterally staggered collagen molecules [98]. A space exists between longitudinally neighbouring collagen molecules, such that the

laterally staggered molecules create regions of ‘overlap’ and ‘gap’. The overlap and gap zones are 27 nm and 40 nm, respectively, which form the 67 nm periodic spacing.

The hydroxyapatite mineral is generally plate-like with dimensions between 50–100 nm in length, 25–50 nm in width and 4–6 nm in thickness. While several models exist to explain the collagen–mineral interaction [99]–[101], it is widely accepted that the mineral is predominately located in the gap zone with it’s c-axis parallel to the long axis of the collagen fibril [99].

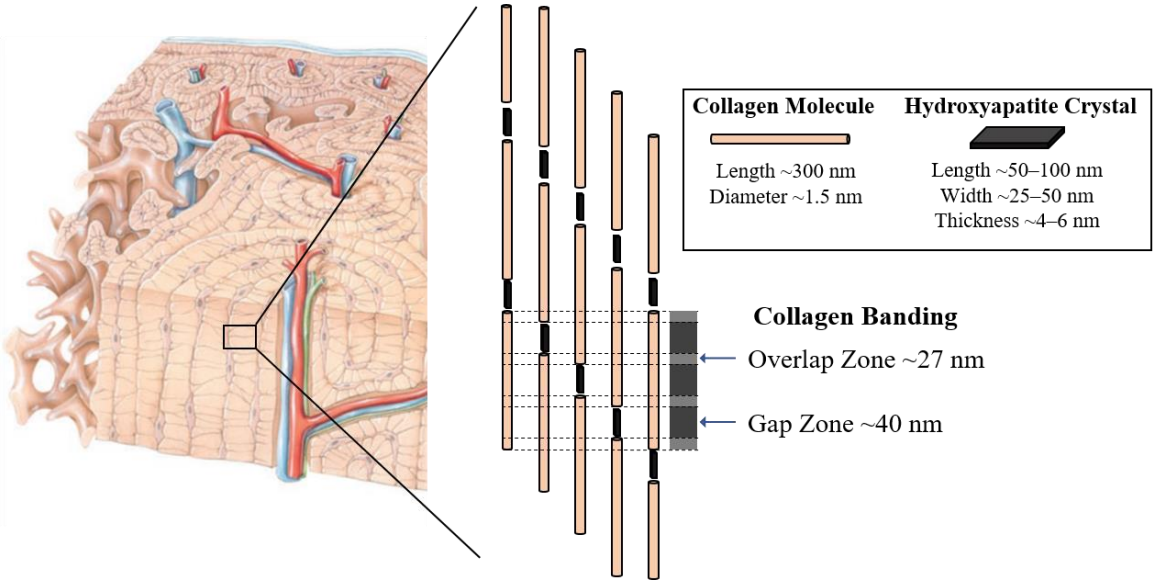

Figure 7. Nanoscale bone structure. Bone lamella are comprised of polymeric collagen and crystalline hydroxyapatite mineral. The collagen and mineral are ordered along the same direction within each lamella, and has a staggered structure, responsible for the periodic banding observed in the TEM. Not to scale.

Histology

Application of a microscope (commonly a light microscope) to the study of biological tissues, with a focus on cell structure and arrangement is termed histology. Histological analysis is best established for imaging *soft* biological tissues. Assessing engineered biomaterials with histology is performed when investigating the interaction of biomaterials with tissues, and commonly involves the removal of the biomaterial from the tissue [102].

A series of thin sections is prepared with the microtome (serial sectioning) providing a 2D representation of the entire specimen volume. The optical system of the light microscope does not produce useful contrast in biological specimens, therefore staining of tissue provides enhanced contrast of specific components [103]. Hematoxylin and eosin (H&E) is the most commonly used stain [104]. Hematoxylin stains DNA in the cell nucleus, RNA-rich portions of the cytoplasm, and the matrix of cartilage, producing a dark blue or purple color. In contrast, eosin stains other cytoplasmic structures and collagen pink.

In addition to micro-CT and electron microscopy, histology with light microscopy was used to complement the observations of the bone response, providing a cellular perspective to the bone-implant interaction.

Methods and Materials

Implants

Twelve dual-stemmed implants (herein referred to as the SIT implant) were received from Stemmed Implant Technologies Incorporated (Niagara Falls, Canada). The implants were produced via DMLS using an EOSINT M 280 (EOS GmbH, Kraaling, Germany) printer with Ti6Al4V powder. The 3D printed implants had a 3 mm diameter body, with 1 mm diameter stems. In preparation for implantation, implants were cut to 6 mm in length, briefly sandblasted with 70 psi and a 90% glass bead/10% Al_2O_3 media, and autoclaved. Final implants had body and stem lengths of 3 mm (Figure 8A). Four conical stainless steel mini-implant screws, with a tapered body and maximum diameter of 2 mm were used as controls. The control implants were received from Stemmed Implant Technologies, cut to a 6 mm length to match the length of the stemmed implants (Figure 8B), and autoclaved for sterilization prior the implantation procedure.

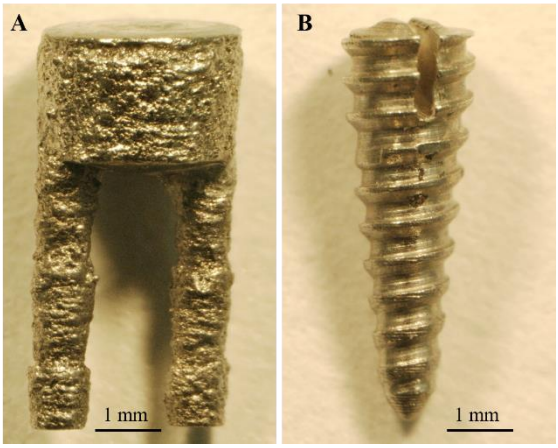

Figure 8. Stereograph images of (A) control conical implant (Ø = 2 mm, *l*= 6 mm), and (B) dual-stemmed (SIT) implant (Ø= 3 mm, *l*= 6 mm).

SIT Implant Characterization

The topography of the SIT implant was assessed using a JSM-6610LV SEM (JEOL Ltd., Tokyo, Japan) SEM in secondary electron imaging mode at 15kV. Surface roughness measurements were carried out using a Formtracer CS-5000 (Mitutoyo Canada Inc., Mississauga, Canada) stylus profilometer with a 5 µm diamond tip. Average surface roughness (R_a) measurements were acquired over the 3 mm length of the SIT body (n=9).

The oxide composition and thickness was determined via an Auger electron spectroscopy (AES) depth profile, using a JEOL JAMP-9500F (JEOL Ltd., Tokyo, Japan) field emission Auger microprobe. The electron and Ar sputtering guns were operated at 10 kV and 1 kV, respectively. The current density of the Ar ion beam was 0.1 mA/cm^2. The oxide thickness

was calculated using the equation: $d = s_R t$ where d is the oxide thickness, s_R is the sputter rate, and t is the sputter time at which the oxygen and titanium atomic concentrations intersected [105]. The sputter rate was determined using the equation: $S_R = \left(\frac{M}{\rho N_A}\right)\left(\frac{S j_p}{e}\right)$ where M and ρ are the molar mass and density of Ti, respectively, e is the electron charge, S is the sputtering yield, and j_p is the ion current density [105]. The sputtering yield (S) was assumed to be 1 atom/ion [106], and sputter rate determined to be 6.5 nm/min.

Implant Placement and Retrieval

Eight skeletally mature female specific pathogen free New Zealand White Rabbits (Charles River, Toronto, Canada) weighing between 3-4 kg were housed at the Central Animal Facility at McMaster University. Animal experiments were carried out under ethical approval (AUP 14-12-54) from the McMaster Animal Research Ethics Board. The day prior to surgery and over the following four days all rabbits received 10mg/kg entrofloxacin (Baytril®) to prevent infection. During surgery, the rabbits were induced with xylazine, ketamine, acepromazine, intubated and placed on isoflurane gas 2-3% inhalation with oxygen. Buprenorphine was administered at 0.5mg/kg subcutaneously to prevent pain and re-administered every 12 hours for 48 hours post operatively. The surgical method was a cranial medial approach parallel to the tibial crest with a slow-rotating drill and irrigation with saline (Figure 9). One implant of each type was inserted into the tibial metaphysis of each rabbit; where stemmed implants were pressed to fit, and conical implants were screwed in until flush with the bone crest. Incisions were closed with a layer of 4-0 Vicryl® and the skin was closed with stainless steel wound clips. Animals were then randomly split into two groups: one provided a 3-week healing period, and the other 12-weeks. After the healing period, rabbits were euthanized by overdose of Barbiturate. However, one animal at each time point was perfused with 2% glutaraldehyde in 0.1M sodium cacodylate buffer solution and bone-implant sections were removed for decalcification with EDTA for histology.

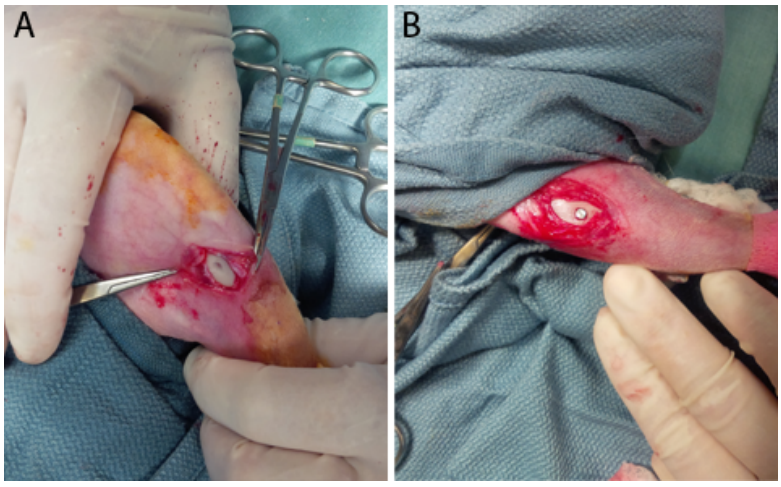

Figure 9. Cranial medial surgical approach parallel to the tibial crest. (A) Slow-rotating drill used to create pilot hole perpendicular to bone crest. B) SIT implants were press fit into place until flush with bone crest. Control implants were screwed into place (not shown).

Implants with surrounding bone tissue were collected and prepared into implant-bone blocs following the methodology for preparing undecalcified bone outlined by Donath and Breuner [107]. Approximately 2 cm x 2 cm bone blocks containing the implants were fixed in a solution of 1% glutaraldehyde and 1% paraformaldehyde in 0.1M sodium cacodylate buffer for 7-10 days, and subsequently dehydrated in a graded series of ethanol (50-100%), followed by embedding in LR White acrylic resin for the 3-week specimens, and Embed-812 epoxy resin for the 12-week specimens. Blocs were longitudinally sectioned using an Isomet® low-speed saw (Buehler, Lake Bluff, USA) and diamond wafer blade to reveal the bone-implant interface.

Histology

Rabbits were sacrificed with 65 mg/kg body weight sodium pentobarbital I.V. and perfused via the left cardiac ventricle with 1 L lactated Ringer's solution followed by 1 L formalin (10% paraformaldehyde in phosphate buffer, pH 7.2). The fragment of the tibial bone with the metal implant was carefully removed, post-fixed in formalin for two days and then placed in formalin supplemented with 4% EDTA for demineralization. Demineralizing solution was exchanged once per week over nine months. The metal implants were carefully removed from the soft bone and the bone was sectioned for analysis at the site of the implants. The sections were dehydrated with a series of graded concentrations of ethyl alcohol (50-100%) and xylene, embedded in paraffin wax, cut 5 μm thick, mounted onto glass slides and stained with both hematoxylin and eosin. The histological analysis was performed under an Eclipse 50i light microscope (Nikon, Tokyo, Japan). The cellular bone response was assessed by observation and comparison of osteoblast and osteoclast presence after 3 and 12 week of healing.

Micro-Computed Tomography

Visualization of whole implant bone in-growth (prior to sectioning) was achieved using a Skyscan 1172 (Bruker, Billerica, USA) micro-CT scanner at 100 kV and 100 μA, with an aluminium-copper filter, 9000 ms exposure time, and 0.3 – 1° rotation step over 360°. NRecon software (Bruker, Billerica, USA) was used to reconstruct the orthoslices using the Feldkamp algorithm [108] with an isotropic voxel size of 2.3 – 2.6 μm^3. At this resolution, the entire implant and surrounding bone were visualized within the field of view of the scanner. CTAn software (Bruker, Billerica, USA) was used to visualize the orthoslices. New bone was differentiated from bone existing prior to implantation by a noticeable decrease in intensity (contrast difference) of the new bone compared to the pre-existing bone. Volume rendering and 3D visualization was performed using Avizo software (FEI, Hillsboro, USA). The amount of new bone growth as a percentage of total bone (percent new bone to total bone) neighbouring the implant was determined using longitudinal orthoslices which contained the entire implant length in the image (Figure 15A). Total cortical bone (TCB) was defined as the length of bone from the top of the implant to the lowest position on the implant for which bone was adjacent. New cortical bone (NCB) was defined as the length of bone underlying the pre-existing bone from which a noticeable intensity change occurred, to the lowest position on the implant for which bone was adjacent. Measurements (n=6) were made using the software ImageJ (National Institutes of Health, Bethesda, USA) for each implant type and at each time point.

Scanning and Transmission Electron Microscopy

Longitudinal implant-bone blocs were coated with gold and imaged with a JSM-6610LV SEM at an accelerating voltage of 10 kV. BSE images with compositional contrast enabled identification of implant, bone, resin, and voids, as the brightest to darkest regions, respectively. Bone-implant integration was investigated along the implant length by inspection for contact or separation. Separation was defined as the presence of either resin or voids between bone and implant.

Transmission electron microscopy specimens were prepared using an *in-situ* lift-out method on a NVision 40 (Carl Zeiss GmbH, Germany), a dual-beam instrument comprised of a focused ion beam (FIB) milling instrument and a Schottky Field Emission Gun filament SEM. Due to implant-bone separation caused during retrieval and sample preparation, an intact bone-implant specimen was not possible. However, bone specimens adjacent to the implant at both the 3 and 12 weeks time points were successfully prepared for analysis. TEM images were captured using a Titan 80-300 (FEI, Hillsboro, USA) TEM operated at 300kV with a high-angle annular dark-field detector. Bone development over time was investigated by comparing the bone morphology at both 3 and 12 weeks of healing.

Results

Implant Characterization

The surface of the SIT implant prior to surgical insertion contains characteristic surface features representative of the powders used in its production. The body and stems are considerably rough (Figure 10), and at higher magnification, circular nodules about 50 μm in diameter, reminiscent of the titanium powders, are observed (Figure 10B). The surface roughness (R_a) was measured to be 18.6 ± 5 μm.

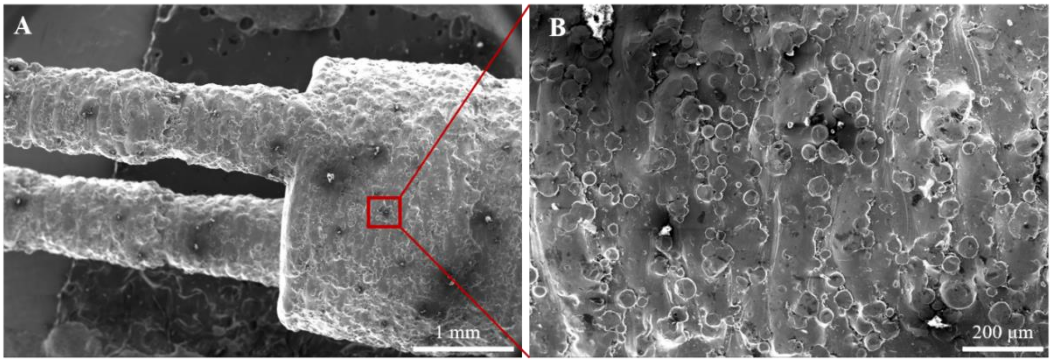

Figure 10. Scanning electron micrographs of the dual stemmed SIT implant. The surface retains features of the powders used in its production (B).

The Auger electron spectroscopy profile of the SIT implant surface showed a high initial content (~60%) of oxygen which quickly decreased with sputter time (Figure 11). A tetravalent titanium content initially half of the initial oxygen content was also detected and decreased with sputter time. As the oxygen and tetravalent titanium content decreased, the

concentration of metallic titanium increased. Additionally, the profile showed approximately 5% aluminum and vanadium throughout the entire sputtered length. The oxide thickness was calculated to be approximately 16 nm.

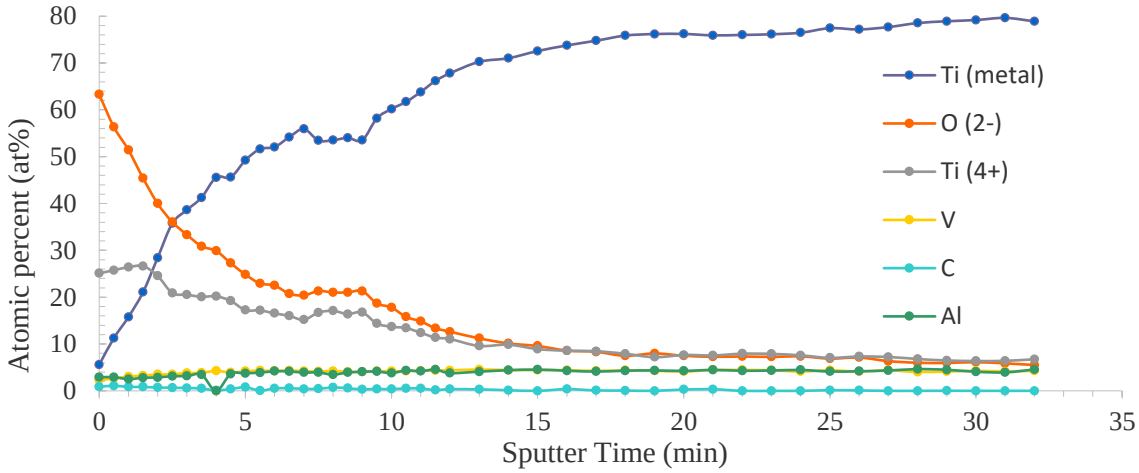

Figure 11. Auger electron spectroscopy (AES) sputter profile of the SIT implant surface.

Histology

Histological analysis of both SIT implants and control screw implants were completed after 3 and 12 weeks of implantation to determine the cellular activity and remodelling behaviour of the bone tissue with the implanted devices (Figure 12). For both the SIT and control groups, implants resided primarily in the cortical bone. Following extraction of the control implant after 3-weeks bone debris was present between the implant and the cortical bone (Figure 12A). This is in contrast to the cortical bone surrounding the SIT implant after 3 weeks, where there was no debris and the presence of multinucleated osteoclasts and hypertrophied osteoblasts suggested the bone was being actively remodeled around the implant (Figure 12D & E). After 12-weeks of implantation, both the control (Figure 12B) and SIT (Figure 12F) implanted rabbits were observed to have active bone remodeling at the bone-implant interface. The control implants showed active bone remodeling involving osteoclasts (Figure 12C), meanwhile, the SIT implant was completely encased in cortical bone, with a layer of bone forming over its surface. The remodelling of the bone was still active, but showed the morphology of more mature bone (Figure 12H).

Micro-Computed Tomography

Prior to sectioning for SEM, the entire implant-bone blocs of the SIT and control implants were imaged by micro-CT. Radiographs of both implant types revealed the top portion of the implants to be surrounded by cortical bone only, with the remainder the implant located in the medullary cavity (Figures 13A, 13E, 14A, 14E). The SIT and control implants were shown to have new bone growing from the pre-existing cortical bone, down and around each implant surface and into the medullary cavity, after 3 and 12 weeks (Figures 13 & 14). Three-dimensional renderings (Figures 13B, 13F, 14B, 14F) of both implants provided a holistic perspective of the entire implant and surrounding bone volume. The new bone growth around the implants is simultaneously visualized with the growth down the implant length. The

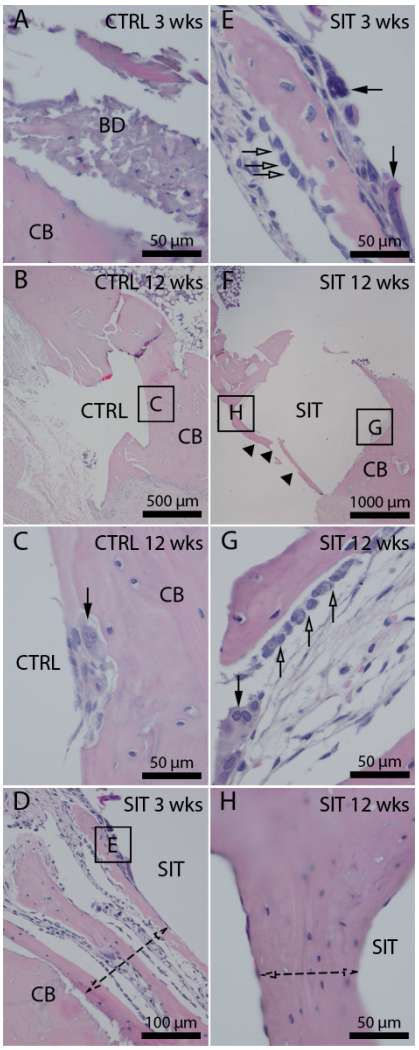

Figure 12. H&E staining highlights histological changes in the tibial bone after implantation of the SIT implant (D, E, F, G, H) or control (A, B, C) for a duration of 3 weeks (A, D, E) or 12 wks (B, C, F, G, H). The metal implants have been removed. (A) At 3 weeks post implantation bone debris is present between the control implant and cortical bone. (B) At 12 weeks post implantation the cortical bone surrounding the control implant has active bone remodeling at the bone-metal interface (C) which involves osteoclasts (arrow). However, the cortical bone is being actively remodeled (double-headed arrow) around the site of the SIT implant (D) after 3 wks. At higher magnification (E), multinucleated osteoclasts (black arrows) and hypertrophied osteoblasts (white arrows) participate in bone remodeling. (F) At 12 wks post-implantation, the SIT implant is encased in the cortical bone (arrowheads) which at higher magnification (H) has the morphology of a mature bone (double-headed arrow). The remodeling of the bone surrounding the SIT implant is still active (G), and involves osteoclasts (black arrow) and hypertrophied osteoblasts (white arrow). CTRL=control, SIT=stemmed implant, CB= cortical bone, BD= bone debris.

location of the reconstructions shown in Figures 13 and 14 are represented in the 3D renderings by the corresponding cross sectional and longitudinal planes. At 3 weeks, the new bone is in an immature state, identified by lighter contrast and porous structure when compared to the pre-existing cortical bone for both the control (Figure13C, 13D) and SIT (Figures 13H, 13G) implants. Qualitatively, through 12 weeks the new bone appeared to have developed into mature or remodelled cortical bone with higher levels of mineralization as a result of the similar contrast and density of the new and old cortical bone for both implant types (Figures 14C, 14D, 14H, 14G). The longitudinal sections of the control (Figure 13C, 14C) and SIT (Figure 13G, 14G) implants showed a difference in the extent of bone growth extending from the bone crest down the length of the implant at both time points. New cortical bone accounted for 25% and 50% of the total bone length residing along the control and SIT implant surfaces, respectively, at 3 weeks (Figure 15). After 12 weeks, new bone accounted for 35% and 55% of the total bone length residing along the control and SIT implant surfaces, respectively (Figure 15). While the bone growth down the SIT implant surface was greater than the control at both time points, a difference in the extent of radial bone growth between the control and SIT implants was less evident.

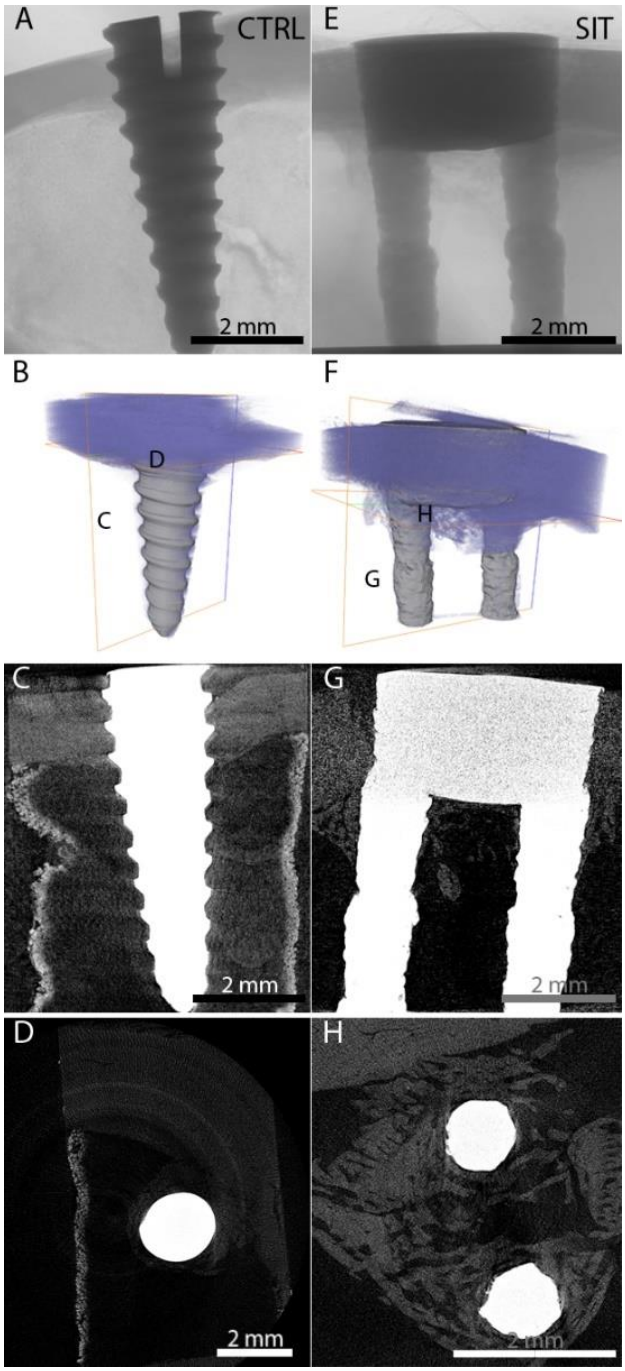

Figure 13. Micro-CT analysis following 3-wk implantation of CTRL (left column) and SIT (right column) implants. (A,E) Radiograph of each implant type. (B,F) 3D visualization of implant and bone (purple) with orthogonal planes labelled, (C,D,G,H) corresponding orthoslices from (B,F) where new bone formation, that appears lighter in contrast, is noted. Both implants showed bone conduction down the implants from the cortical bone crest, while the SIT implant also showed new bone formation between the implant stems.

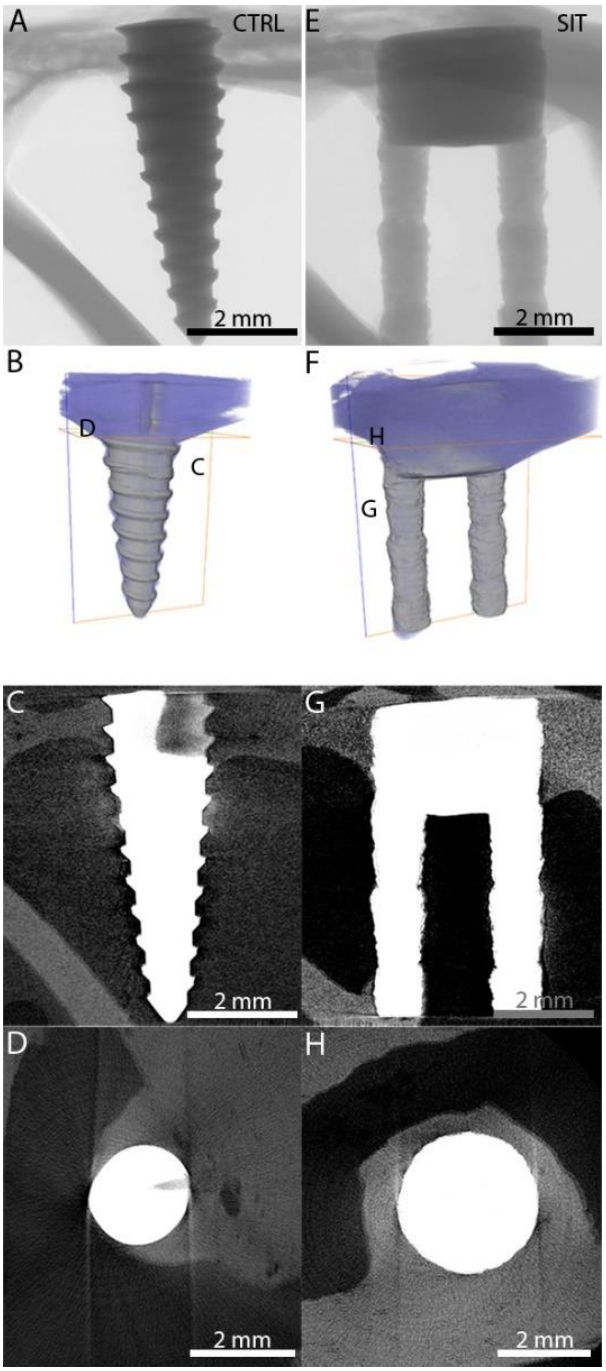

Figure 14. Micro-CT analysis following 12-wk implantation of CTRL (left column) and SIT (right column) implants. (A,E) Radiograph of each implant. (B,F) 3D visualization of implant and bone (purple) with orthogonal planes labelled, (C,D,G,H) corresponding orthoslices from (B,F) where the new bone has matured and is of equal intensity to the pre-existing bone. Both implants showed bone conduction down the implants from the cortical bone crest, however bone growth between the stems was not noted in this particular specimen.

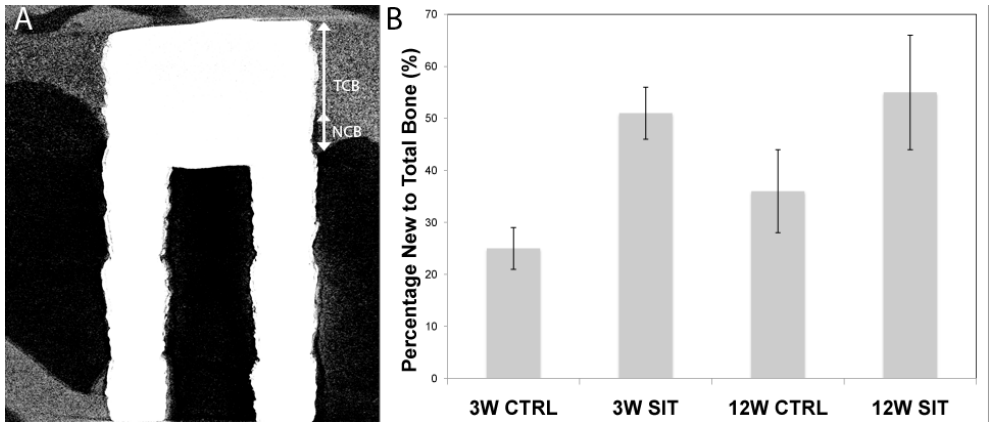

Figure 15. (A) Representative micro-CT orthoslice of SIT device, indicating new cortical bone growth (NCB), and total cortical bone (TCB) from the coronal surface after implantation. (B) Graphical comparison of new bone formation under the cortical bone crest to total bone crest height observed after 3- and 12-wk implantation for control and SIT implants.

Scanning Electron Microscopy

Similar to the micro-CT results, SEM images did not show a trabecular bone transition underlying the cortical bone, which indicated some misplacement of the implant off the target anatomical position. As such, bone contact was only possible originating from the cortical bone crest. Imaging of the embedded sections with SEM enabled qualitative assessment of BIC in this cortical region. Three weeks after implantation cortical bone was present within the threads of the control implant (Figure 16A). This mechanically interlocked bone was in contact with the control implant, while new bone further down the length of the implant was primarily not in direct contact. However, stress cracks were observed at the mechanically interlocked thread tips. In contrast, little to no bone was in contact with the SIT implant after 3 weeks (Figure 16C). The absence of threads also indicates a lack in mechanical interlocking. The bone structure around the SIT implant specimens appeared less developed with more porosity and randomly oriented osteocyte lacunae; however, in some cases new bone formation was observed in-between the stems of the SIT implant. Twelve weeks post-implantation, the bone surrounding both implant types was more developed and in greater contact with the implant surfaces (Figure 16B and D). The arrow in Figure 16D points to bone growth within the micro-porosities of the SIT implant suggesting improved osteoconduction. As with the 3 week samples, stress cracks were also present within the bone from the 12-week control implant.

Transmission Electron Microscopy

To fully assess the osseointegration between bone and implant and the quality of bone tissue at the interface, higher resolution than that achieved by SEM is required. Figure 17A shows a STEM image of the SIT implant-bone interface after 12 weeks of healing. A separation at the bone-implant interface, likely due to mechanical stresses during removal and resin infiltration, was exaggerated by the FIB during TEM sample preparation. However, the matching contours of the bone and implant surface indicate that the implant and bone were likely in complete contact prior to retrieval. Preparation of a TEM specimen for the SIT implant at 3 weeks was not possible because of a lack of contact at the bone-implant interface.

However, a specimen of bone near the implant interface was removed for TEM. The difference in bone quality near the implant surface at 12 and 3 weeks is shown in Figure 17B and C, respectively. The collagen fibers of the 12-week bone are more organized compared to the woven collagen fibers and visible mineral clusters of the 3-week bone, highlighting the differences in bone maturity.

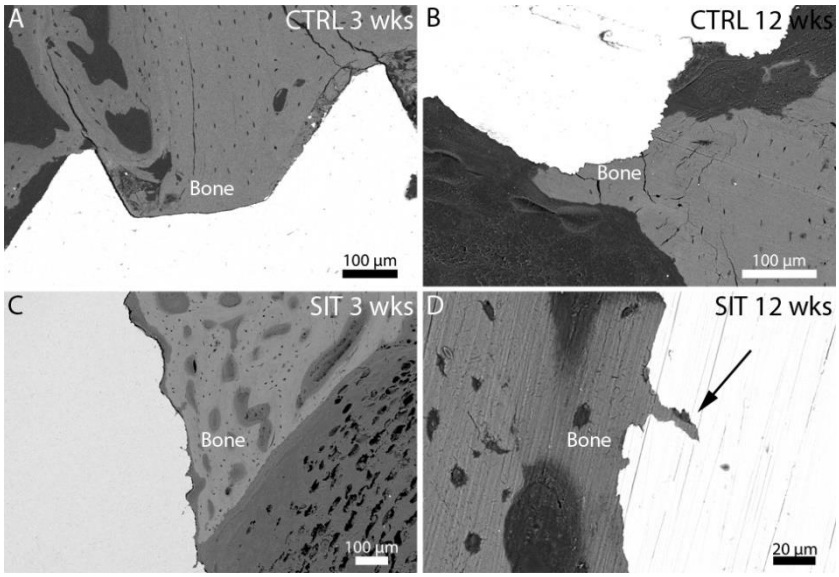

Figure 16. BSE-SEM images of the bone-implant interface after 3 (A,C) and 12-wk (B,D) implantation for (A,B) control and (C,D) SIT devices. Bone conduction along and into the micro-porosities of the SIT implant were observed after 12-wks (arrowhead).

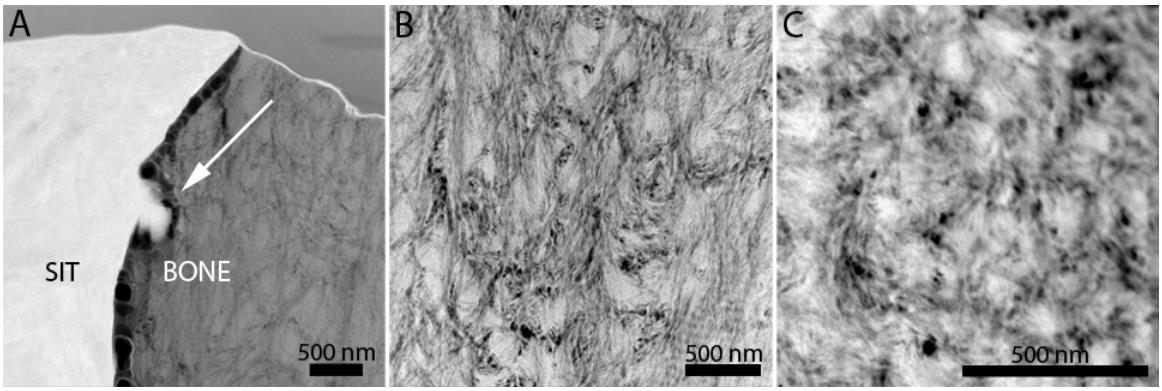

Figure 17. HAADF STEM images of (A) the SIT implant-bone interface after 12-wks implantation. Bone growth around the nanoscale features was observed (arrow). (B) Ordered collagen fibrils, representative of mature bone, are noted adjacent to the implant at 12-wks, while at 3-wks implantation (C) partially disorganized collagen fibrils, representative of newly developing woven bone, are noted adjacent to the implant, consistent with new bone structure.

Discussion

A novel dental implant design by Stemmed Implant Technologies Inc. is marked by a significant geometrical change that employs dual prong-like stems when compared to conventional implants that are generally conical threaded screws. The biocompatibility of any load bearing implant is largely dependent on the surrounding bone response. Understanding the bone-implant interactions of the SIT implant is a crucial assessment for assessing biocompatibility, and to predict its potential success in clinical scenarios. This was conducted by comparing the bone response of the SIT implant to a conventional threaded implant with histology, X-ray and electron microscopies.

Characterization of the SIT implant prior to implantation revealed a rough surface with circular features due to the partial sintering of particles through the DMLS process [109]. Surface roughness is an important property of dental, and other load bearing, implants because the response of bone to the implant is largely controlled by the nature and texture of the surface of the implant. Compared to smooth surfaces, rough implants surfaces exhibit more interfacing surface area for integration with bone [54]. Micro-roughness, ranging from 1-100 μm has been shown to improve the growth, and interlocking, of bone at implant interfaces [55], which the measured SIT implant surface roughness was within (Ra = 18.6 μm). The DMLS process provides an inherently positive surface topography on the SIT implant for bone growth and integration. In addition, titanium spontaneously forms a passive TiO_2 oxide layer when exposed to air, which can reach a thickness up to 20 nm [110]. This stable surface oxide layer of titanium is biocompatible [111], provides high corrosion resistance [112], and osseointegrates with bone [113]. Auger electron spectroscopy of the SIT implant revealed an elemental surface composition representative of TiO_2, supporting the observed integration of the SIT implant with bone.

Histological analysis showed active bone growth and remodelling for both the SIT and control implants via osteoclast and osteoblast mediated bone matrix resorption and deposition. These observations are similar to previous histomorphometric evaluations of other DMLS implants placed in both sheep and humans [114], [115]. The observation of bone debris for the control implant at 3 weeks and predominant osteoclast activity at 12 weeks compared to the SIT implant suggests a potential difference in the rate of bone formation and remodelling between the implants. Bone debris in the peri-implant space at early healing time points has been observed previously with threaded implants [115], [116], and may lead to delayed bone formation compared to implants devoid of threads [117]. Histological analysis indicates that the SIT implant shows comparable cellular response to conventional implants after 12 weeks, marked by complete bone encasement and active remodelling.

The non-destructive basis of micro-CT has been demonstrated as a useful tool for visualizing the entire implant and bone volume in 2D and 3D. Contrast gradients enable differentiation of new bone from old bone, and identification of active remodeling sites, as well as sites lacking bone and osseointegration. These micro-CT results indicate that the implants were only anchored in cortical bone, despite the usually large amount of trabecular bone present in the metaphysis of rabbits where implants were placed, indicating a potential misplacement.

A relatively small amount of bone growth was conducted from the cortical bone crest down the implant length for the control implant, compared to a slightly larger amount on the SIT implant that was even clearly visible between the implant stems at 3 weeks. Ideally, placement in trabecular bone would maintain bone trabeculae between the stems for added stability. The reason for the observed difference in bone growth is somewhat unclear due to the potential interplay between differences in both the osteoconductivity of titanium and steel, and the radial bone growth required for the control implants due to the threaded design. By three weeks the majority of the bone volume, which was to encapsulate the implants, had been deposited and was remodelled into more mature dense bone, but not a greater quantity, by 12 weeks. The observed gross bone response to the SIT and control implants is in agreement with the time frame reported for wound healing around dental implants, where deposition and growth of immature bone tissue is normally laid down between 1-4 weeks, followed by maturation and strengthening from 6-12 weeks [118].

While micro-CT is ideal for a general overview of bone growth, it lacks the resolution necessary to visualize submicron features at the BIC. The greater extent of bone growth from the cortical region down the implant surfaces for the SIT implant was confirmed by SEM. The SIT implant conducted bone growth along its length, and within the stems. The control implant initiated a limited amount of new bone formation and large cracks were present within the cortical bone, perhaps caused by over-torqueing during implant placement. Very tight integration, with no separation was seen around the SIT implant after 12 weeks, as the bone had grown into the micro-pores of the implant surface, an indicator of biocompatibility. Comparison of BIC across studies remains challenging because of a lack of standardized methodologies employed to model bone growth and measure BIC. Animal model selection, bone type, surgical procedure, heal time, sample preparation methodology, and selected implant length for BIC measurements varies across studies, all of which can influence the BIC [34], [60], [115], [119]. Never-the-less, previously reported BIC measurements of a machined and analogous 3D printed implants after 2 weeks was 20% for both implant types [115], supporting the low bone-implant contact of the SIT implant at 3 weeks. We instead looked at the conduction of bone down the implant surface, since it was placed primarily in cortical bone, and found as expected, the titanium SIT implant was a better conductor of bone growth at both early and late time points.

Due to bone-implant interface separation caused by FIB sample preparation, the exact integration between the bone and the SIT implant could not be analyzed; however, the maturity of the bone surrounding the implant could be evaluated to demonstrate the success of bone growth at the implantation site. TEM imaging revealed differences in the orientation of the collagen fibrils and presence of mineral clusters after 3 and 12 weeks. This suggests that the mechanism of distant osteogenesis is occurring during healing after the insertion of the implants. In distant osteogenesis, mature bone acts as a substrate for osteogenic cells to form a matrix that gradually encroaches upon the implant surface [120].

This pilot study was limited to an investigation of the structural and biochemical interaction of the implant device *in vivo* via advanced imaging modalities. To further validate these results, future work should focus on determining the mechanical integrity of the bone-implant interface. Mechanical testing of the implanted devices would also be beneficial to improving

the understanding of the overall system. This could be completed *in vivo* through methods such as resonance frequency analysis to determine implant stability [121], and via pull out tests to confirm adequate mechanical strength [122]. Complementary information from *in vitro* testing, such as investigating cell viability [123], may provide additional insight into the biocompatibility of the device. Other works reporting 3D-printed implant devices have shown promising cell viability and biocompatibility [124]–[126].

Conclusion

The first step in investigating the functional ability of this dual stemmed design is to ensure the bone response, at the least, is equivalent to current in use implants. Initial observation of the SIT dental implant has shown successful bone growth and bone-implant contact similar to conventional and other 3D printed implants up 12 weeks of healing in rabbits. A desired cellular response was achieved, as bone cells were observed in the proximity of the implant, with no observation of inflammation or rejection. In some cases, new bone formation was noted in between the stems of the device, although the stems were not within a trabecular bone region. The conventional implants showed mechanical interlocking, but did have indications of stress cracking and bone debris. Further work to assess the *in vivo* mechanical stability and response of this implants is needed. The three-dimensional and high-resolution imaging acquired with complementary micro-CT and electron microscopy demonstrates that this implant design is suitably biocompatible, as it allows for successful osseointegration in rabbits up to 12 weeks, and supports additional *in vivo* experiments aimed to; improve the statistical significance of the current research, improve the bone model, and demonstrate the mechanical properties of the implant.

CHAPTER 3: CHARACTERIZATION OF A GOLD FUNCTIONALIZED COLLAGEN SCAFFOLD

Motivation and Aims

An essential aspect of biomaterial research is the demonstration of biomaterial function *in vivo*. This type of study was presented in Chapter 2. To assess the bone-implant interface, the rabbits were sacrificed, and the implant with surrounding bone was removed for study. This type of *ex vivo* analysis is a commonly applied methodology to study implant biomaterials [127]–[129], but leads to significant ethical implications and increased variability within data. Conversely, non-invasive imaging using X-ray, fluorescence, and ultrasound are currently applied techniques to monitor and study biomaterial and tissue function [130]–[132], however, they are not without limitation.

Detection and quantification of fluorescence has been demonstrated as a potential technique to measure biomaterial degradation [131], however the achievable penetration depth of light limits detection to subcutaneous locations [133]. X-rays have a much deeper penetration depth within tissues, and therefore presents as a superior technique to measure biomaterial degradation non-invasively, but suffers from poor soft tissue contrast (e.g. collagen) [134]. However, contrast enhancement with heavy elements for X-ray CT imaging of soft tissues provides a means to overcome contrast limitations [135].

In a collaborative effort to test the potential of non-invasive, *in vivo* X-ray CT imaging, a collagen scaffold has been fabricated in the lab of Dr. Ryan Roeder at the University of Notre Dame (Indiana, USA) as a model for the detection and quantification biodegradation, *in vivo*. Collagen is a well-known and studied biomaterial with potential in many biomedical applications such as skin [136], bone [137] and nerve repair [138], and is therefore an appropriate scaffold model. An understanding of scaffold biodegradation is important for the improved design and success of biodegradable biomaterials. To improve the detection of collagen by X-ray CT, the scaffold has been functionalized with gold nanoparticles as a contract agent. Gold nanoparticles are a commonly used X-ray contrast agent for *in vivo* applications, exhibiting strong X-ray contrast and biocompatibility [139].

Characterization of the fabricated gold functionalized collagen scaffold is important to understand and interpret the X-ray CT data acquired during degradation experiments.

This chapter investigates the structure of a gold functionalized collagen scaffold using complementary X-ray and electron microscopy. The aims of this study were to:

1. Develop appropriate methods to evaluate the 3D scaffold porosity and gold nanoparticle distribution
2. Characterize the scaffold porosity and gold nanoparticle distribution

Background

Electron Tomography

Electron tomography (ET) is an advanced 3D imaging technique used to image materials with the resolving power of the TEM, while overcoming the projection limitation of conventional TEM and STEM images. The principle of ET is analogous to micro-CT, by acquiring a series of projection images at various rotation/tilt angles, the entire volume of the specimen can be reconstructed and visualized in 3D. An important difference between ET and micro-CT is the achievable tilt range during acquisition. Where 180-360° rotation is readily achieved for micro-CT, the geometry of the specimen holder for TEM limits conventional ET tilt ranges to a maximum of 140° (-70° to +70°) [140]. The implication of this is an artifact known as the *missing wedge* [140], which causes the artificial elongation of objects in the depth (z) direction because of a lack of projection information (Figure 18).

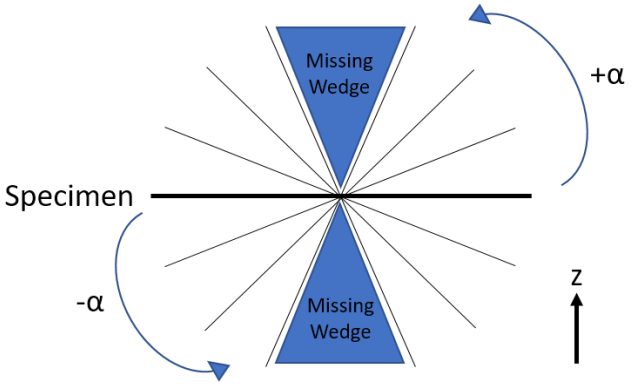

Figure 18. Missing wedge. The achievable tilt range (-α to +α) during acquisition is dependent on the TEM sample holder and position of the sample within the copper grid. The space not sampled is called the missing wedge and leads to elongation artifacts. The axis of rotation is into the page.

The contrast achieved in the TEM projections is also important because to satisfy the projection requirement for reconstruction the contrast must depend only on mass-thickness effects [141]. This is the main determinant of contrast for X-ray imaging, however diffraction contrast can also occur during election microscopy, creating artifacts in the resultant reconstructions. Therefore, unless ET is being performed on an amorphous material, HAADF STEM is the preferred acquisition mode due to its ability to suppress diffraction contrast.

Another difference between micro-CT and ET is the requirement to align the acquired projections prior to reconstruction. Random movement of the specimen during acquisition will shift the same object in sequential projections with respect to the rotation axis. Although random movement is a concern in micro-CT, the effect is less noticeable at the length scale commonly reconstructed, and are therefore easier to correct. Very small disruptions at the nanometer scale will cause large movements within images, causing artifacts in ET reconstructions. Therefore, specific to ET, the projections require alignment prior to reconstruction, this can be achieved manually or computationally [141]. Computational alignments methods are dependent on the ability of the algorithm to identify the same feature at different projection angles. Common computational alignments use a cross correlation

algorithm [142] or fiducial marker tracking [143]. Fiducial marker tracking with distinct NPs is the preferred method for alignment because they are easily tracked [143]. In some cases, gold NPs are added specifically to the sample support grids just for pre-reconstruction alignment [144]. The process of reconstruction and visualization of ET datasets then follows the same principles as micro-CT.

Methods and Materials

Gold Functionalized Collagen Scaffolds

Gold functionalized collagen scaffolds were prepared at the University of Notre Dame in the lab of Dr. Ryan Roeder. The scaffolds were made by a compression loading and porogen leaching process [145]. Briefly, lyophilized type I collagen from bovine tendon (Advanced BioMatrix, Carlsbad, USA) was rehydrated with dionized water (4 mg/mL) and homogenized. Colloidal gold NPs (10mM) to act as contrast agents were prepared in lab following the Turkevich method [146] and functionalized with mercaptosuccinic acid (MSA) to facilitate binding of the NPs to the collagen. MSA-gold NPs were added to the homogenized collagen solution at a volume ratio of 1:2 NP to collagen solution, and vortexed. The gold-collagen mixture was centrifuged to separate the collagen and gold mass from water. Next, paraffin beads (300-425 μm) were mixed with the gold-collagen mass to provide mechanical stability for forming and to act as a poragen. The gold-collagen-paraffin mixture was compression molded into 3x3 mm cylinders. The paraffin beads were then leached out by dissolving the paraffin in a sequential hexane and alcohol (90%) wash, creating the scaffold porosity. Finally, the porous gold-collagen scaffolds were crosslinked with the zero length crosslinker N-(3-Dimethylaminopropyl)-N′-ethylcarbodiimide (EDC) mediated by N-hydroxysuccinimide (NHS). The crosslinking step is two-fold: firstly, it crosslinks the collagen fibrils, enhancing the scaffold strength, and secondly, it crosslinks the gold NPs to the collagen fibrils creating a chemical link between the gold and collagen, which will only be disrupted by enzymatic degradation. Four crosslinked gold-collagen scaffolds were stored and shipped in 1x phosphate buffered saline (PBS). Received gold-collagen scaffolds were fixed with 2% glutaraldehyde in 0.1M sodium cacodylate buffer. An image of an air-dried gold-collagen scaffold is shown in Figure 19.

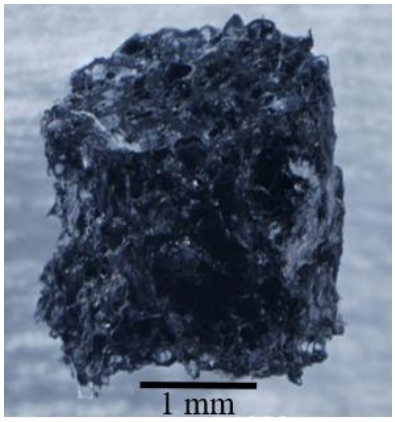

Figure 19. Gold functionalized collagen scaffold. The scaffold has been air dried for imaging.

Micro-Computed Tomography

Visualization of whole gold-collagen scaffolds and porosity was achieved using a Skyscan 1172 (Bruker, Billerica, USA) in both wet and dry conditions. For imaging under dry conditions, scaffolds were dehydrated in a graded series of ethanol (50-100%) over 2 days and critical point dried (Leica EM CPD300, Wien, Austria) in 100% ethanol. A dry scaffold was imaged in air at 34 kV and 210 μA, with no beam filtration, 1100 ms exposure time, and 0.3° rotation step over 360°. NRecon software (Bruker, Billerica, USA) was used to reconstruct the orthoslices using the Feldkamp algorithm [108] with an isotropic voxel size of 2.35 μm^3. At this resolution, the entire scaffold was visualized within the field of view of the scanner. For imaging under wet conditions scaffolds, a scaffold was stained with osmium tetroxide using a 1% osmium tetroxide in distilled water solution, following the protocol outlined by N. Reznikov (2012) [147]. The protocol involved repetitive treatment of the scaffold in osmium tetroxide for 60 minutes, then treatment in 0.5% thiocarbohydrazide in DI water for 30 minutes, followed by an additional treatment of the scaffold in osmium tetroxide for 60 minutes. The wet scaffold was imaged in deionized water contained within a polypropylene (Eppendorf®) tube. Acquisition was performed at 44 kV and 222 μA, with a 0.5 mm Al filter, 950 ms exposure time, and 0.3° rotation step over 360°. NRecon software was used to reconstruct the orthoslices using the Feldkamp algorithm with an isotropic voxel size of 3.42 μm^3. At this resolution, the entire scaffold was visualized in the field of view of the scanner. Volume rendering and visualization was performed using Avizo software (FEI, Hillsboro, USA). Three-dimensional porosity (percent total porosity) was calculated using CTan software (Bruker, Billerica, USA). Percent total porosity is the volume of all open and closed pores as a percent of the volume of interest (VOI). An open pore is defined as any space located within a solid object or between solid objects, which has any connection in 3D to the space outside the object or objects. A closed pore in 3D is a connected assemblage of space (black) voxels that is fully surrounded on all sides in 3D by solid (white) voxels. Prior to the percent total porosity calculation, a VOI was extracted eliminating any space outside the scaffold, and the orthoslice images were converted to binary images using a binary threshold selection including all greyscale values. The binary images were then denoised using a despeckle filter eliminating any object smaller than 75 pixels within each orthoslice. The pore size distribution was determined in two dimensions (2D) and 3D using the orthoslices and volume renderings, respectively. A pore was defined as the space completely or partially surrounded by collagen, which was once occupied by a poragen. Two-dimensional pore size distribution was determined by manual measurement of both the dry (n=1719) and wet (n=1296) scaffolds throughout the volume of interest using ImageJ software (National Institutes of Health, Bethesda, USA). Three-dimensional pore size distribution was determined using the volume rendering (n=502) following instructions outlined in the Avizo software users manual [148]. Prior to volume rendering and calculation, the orthoslices were denoised using a median filter and transformed into binary images using a binary threshold selection including greyscale values to segment the pore space, followed by an morphological opening operation (10 pixel ball kernel) and watershed separation (marker extent = 4) to segment individual pores once occupied by a poragen. The pores were binned and colour coded based on volume. The pore diameters were back calculated assuming the spherical geometry.

Transmission Electron Microscopy

TEM specimens were prepared by dehydrating a scaffold in a graded series of ethanol (50-100%) over 2 days then embedding in epoxy resin (Embed 812®). Eighty nanometer thin sections were cut on a Leica UCT ultramicrotome and picked up onto Cu grids. The sections were post-stained sequentially with a saturated uranyl acetate solution in 50% ethanol for 5 minutes, and Reynold's lead citrate stain [149] for 3 minutes. Sections were viewed in a JEM 1200 EX TEMScan TEM (JEOL Ltd, Tokyo, USA) operated at 80kV. Images were acquired with an AMT 4-megapixel digital camera (Advanced Microscopy Techniques, Woburn, MA). Two-dimensional individual gold NP size (diameter) distribution was determined using BF-TEM images acquired at 100000 – 500000x magnification, and measured manually (n=435) with ImageJ. The 2D NP agglomerate size (area) distribution was determined using BF-TEM images acquired at 50000x magnification, and measured automatically (n=22623) with ImageJ by automated identification of the gold NPs and agglomerates. Prior to calculation the images were transformed to binary images using a binary threshold selection to segment only the gold.

Electron tomography of an 80 nm section was performed with a Titan 80−300 STEM (FEI Company, The Netherlands) operated at 300 kV and convergence angle of 6.24 mrad. HAADF images were automatically acquired via FEI's Explore 3D (FEI Company, The Netherlands) software package for tomography. The sample was mounted on the single-tilt tomography holder, and a tilt-series from −65° to +75° was achieved with images recorded every 2°. The acquired projections were aligned via fiducial marker tracking, and then reconstructed with a simultaneous iterative reconstruction method (SIRT) with 20 iterations in Inspect 3D software (FEI, Hillsboro, USA). Volume rendering and visualization was performed with Avizo software. The NPs and agglomerates were colour coded based on volume. Three-dimensional single and agglomerated NP size distribution was determined by counting the number of single and agglomerated NPs in the volume.

Statistical Analysis

Statistical analysis to compare the pore size distribution of the gold-collagen scaffold in wet and dry conditions was performed using a two sample t-test assuming equal variances ($p<0.05$).

Results

Micro-computed Tomography

An entire gold-collagen scaffold was non-destructively imaged in 3D under wet and dry conditions using micro-CT. In both the wet and dry cases, the reconstructed orthoslices and volume renderings revealed a highly porous scaffold with a heterogeneous pore structure (Figure 20). The shape of the pores viewed with the orthoslices varied from single circles to complex 'multifoil'-like shapes, where multiple overlapping pores produced a series of cusps. The size of the pores also differed in both 2D and 3D (Figure 21).

Low contrast in many regions of the wet scaffold prevented a representable volume rendering and 3D pore size measurements. The 2D pore size distribution of both the wet and dry

scaffolds were normally distributed, with mean pore sizes of 286±64 μm and 201±70 μm, respectively.

The wet scaffold was determined to have a statistically higher average pore size compared to the dry scaffold when measured with the orthoslices ($p<0.05$). The pore size distribution of the dry scaffold measured in 3D was skewed right with a mean pore size of 136±80 μm and median pore size of 115 μm. The 3D total porosity of the dry scaffold was measured to be approximately 80%.

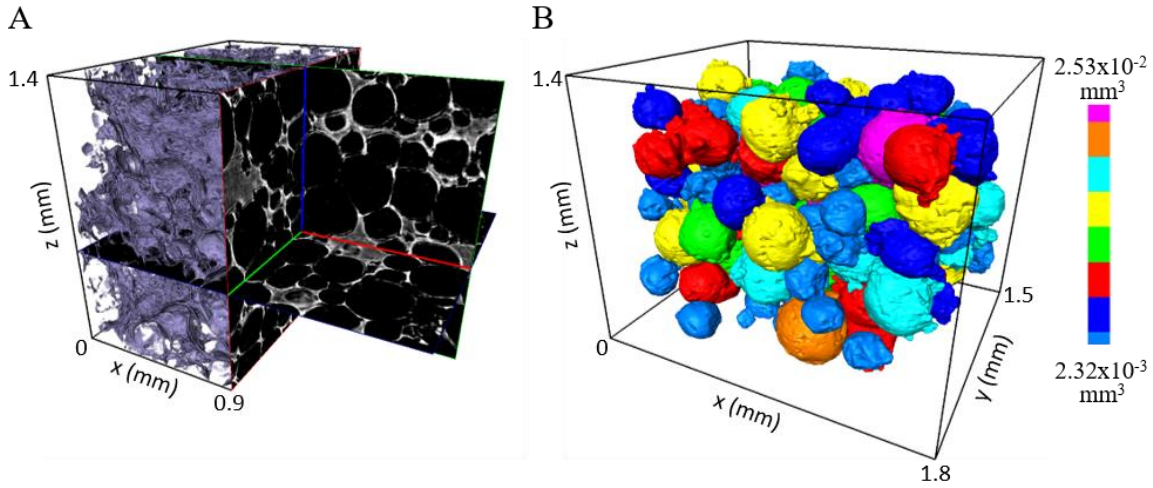

Figure 20. Two- and three-dimensional visualization of a gold-collagen scaffold pore structure imaged in a dry condition with micro-CT. A) Volume rendering and orthoslices in xy, xz, and yz planes, where in 2D white represents the collagen, and black is the pore space. The pores are interconnected and form a multifoil shape, where overlapping pores form cusps. B) Volume rendering of segmented pore structure, with pores coloured according to volume.

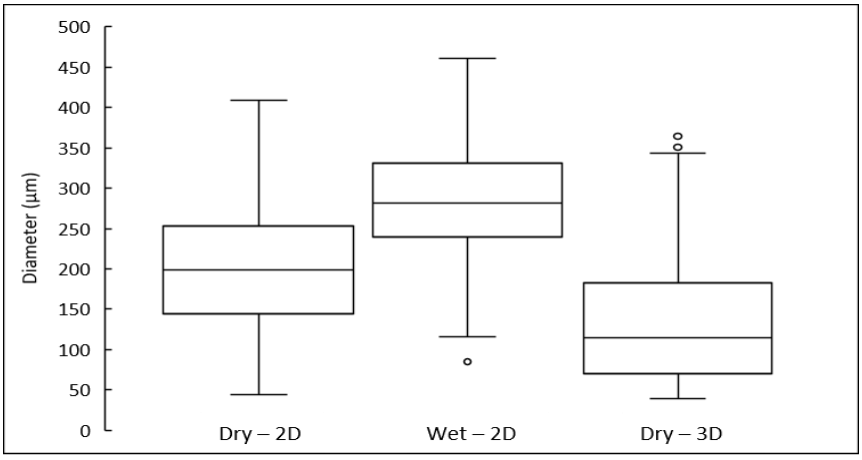

Figure 21. Pore size distribution of gold-collagen scaffolds measured in dry and wet conditions or from 2D or 3D data. The 2D pore size in wet and dry conditions was determined to be statistically different ($p<0.05$), indicating sample shrinkage during drying. 3D pore volumes of a dry scaffold were measured to be smaller on average than a dry scaffold measured from 2D data.

Transmission Electron Microscopy

The gold NP size and spatial distribution was investigated using TEM. BF-TEM images revealed a homogeneous single NP size distribution, but a heterogeneous agglomerate size distribution, and non-uniform NP and agglomerate dispersion (spatial distribution) throughout the sampled scaffold (Figure 23). The size distribution of both single gold NPs and agglomerates are shown in Figure 22. The average size of individual gold NPs was measured to be 15.7±1.6 nm (Figure 22A). Most of the measured NPs had an area representative of a single gold NP (~200 nm^2) (Figure 22B), however, the distribution of was skewed right, representing agglomeration, with agglomerates up to approximately 650 nm^2. The mean particle size (including both single NPs and agglomerates) was measured to be 349±596 nm with a median of 190 nm.

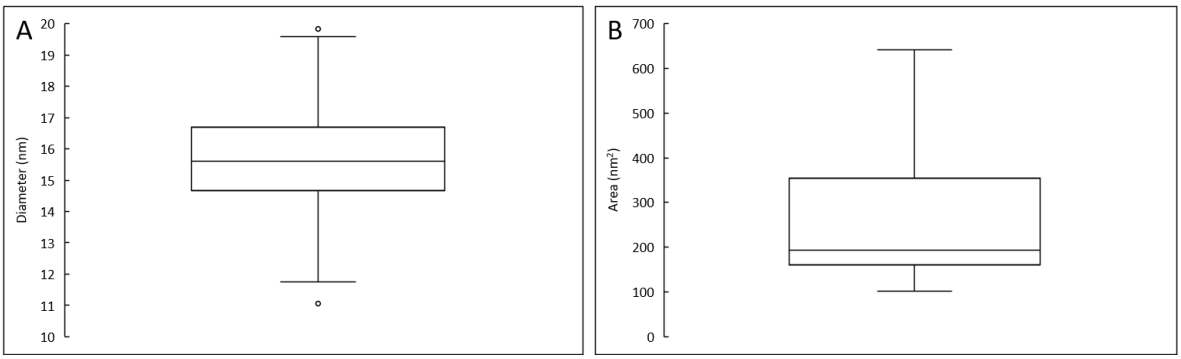

Figure 22. Size distribution of single gold NPs (A) and single plus agglomerated NPs (B), measured from 2D images. The area of a single gold NP is approximately 200 nm^2 with corresponding diameter of 15.7±1.6 nm.

Within the sampled regions, areas of uniform NP and small agglomerate dispersion were observed, although this occurrence was relatively uncommon (Figure 23A). The NP trends typically observed was of variable NP and agglomerate density (Figure 22B-D). Areas of relatively high NP density compared to other near-by regions were observed, and on multiple occasions agglomerates as large as 1 μm were identified (Figure 23B). Conversely, areas of little to no NP presence existed (Figure 23C). In addition, the NPs and agglomerates did not appear to be randomly distributed throughout the collagen, but instead had specific orientations along edges and within sections (Figure 23C & D). The orientation of NPs within areas varied with respect to degree of curvature, where in some cases they were observed to have a curved appearance (Figure 23C) and in others a more linear trajectory (Figure 23D). At high magnification, the size and circular shape of single gold NPs were observed (Figure 23D & E).

Electron tomography of a 750x750x80 nm gold-collagen scaffold region revealed the 3D size distribution of gold NPs (Figure 25). Most NPs were single gold particles with a distribution skewed to the right (Figure 24). Agglomerates ranging from 2 to 10 gold NPs were observed in this small volume.

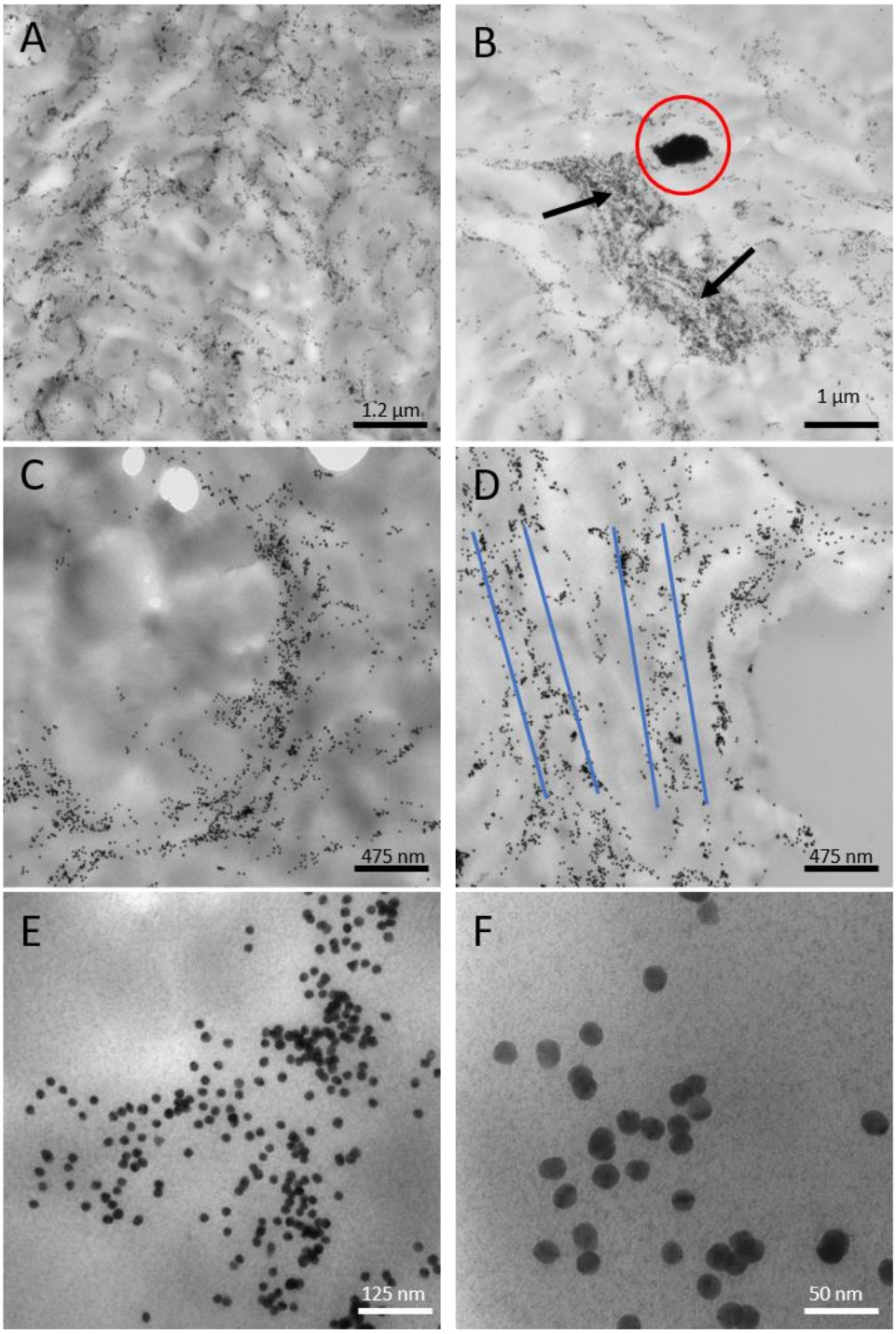

Figure 23. BF-TEM images of a gold-collagen scaffold. Across increasing magnification (A-F) the NP and agglomerate size and spatial distribution are observed. Areas of (A) uniform NP dispersion, (B) high NP density (arrows) and large agglomerations (red circle), (C) little to no NP presence, and (D) non-random NP orientation (blue lines) are observed. The size and shape of single gold NPs are shown (E,F).

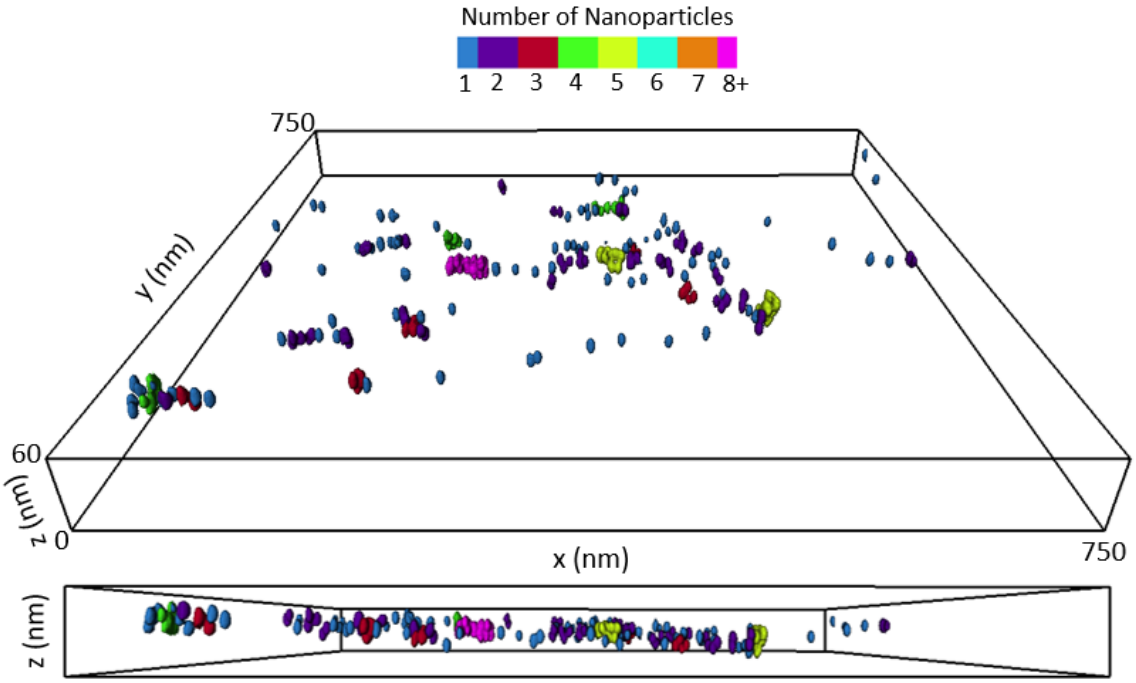

Figure 25. Volume rendering of a gold-collagen scaffold using electron tomography. Single and agglomerated gold NPs are visualized in 3D allowing for the identification of individual NPs within agglomerates. Agglomerates are colour coded based on the number of single gold NPs per agglomerate.

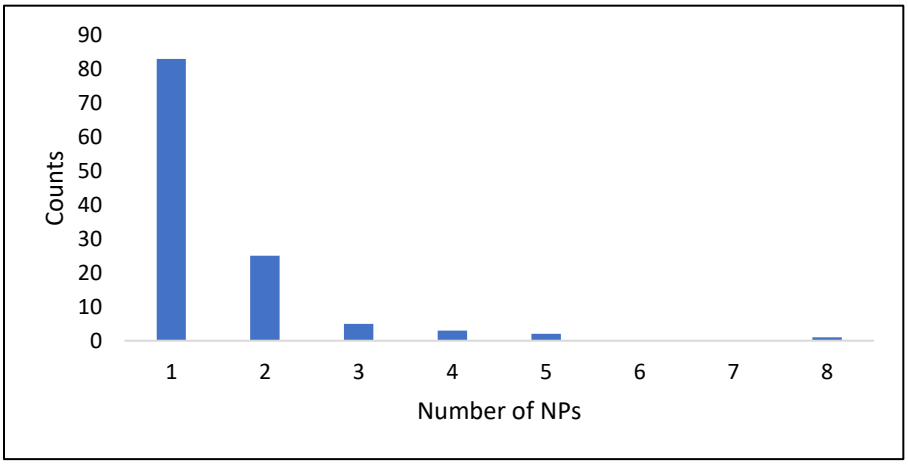

Figure 24. Three-dimensional gold NP clustering measured from the above electron tomography volume rendering. In the section, most particles are single or two NP clusters. This measurement is highly dependant on the region of interest selected.

Discussion

The structure of a gold functionalized collagen scaffold designed at the University of Notre Dame to test X-ray CT as a non-invasive method for the tracking and measuring biodegradation, was characterized using X-ray and electron microscopy.

Micro-CT enabled the non-destructive characterization of the gold-collagen scaffold, revealing a highly porous and interconnected structure. The observation of many multifoil (an architectural term) shaped pores, due to overlapping individual pores, demonstrated the pore interconnection, where approximately 99% of the total porosity was open. The overlapping pores structure is the result of paraffin bead agglomeration during compression loading when the scaffolds are formed.

When imaged in a dry state, the scaffold pore structure was well visualized due to the unimpeded attenuation of low energy X-rays and the presence of the gold NPs. However, drying biological materials results in contraction and volume reduction. Collagen based tissues, such as demineralized dentine have been observed to shrink up to 30% when air dried [150], leaving a state which is not representative of the native structure. Even techniques, such as critical point drying, aimed to limit the amount of shrinkage, still allows a significant amount of reduction. Volume reductions of 19% for lung tissue, 30% for liver tissue, 41% for mouse embryonic tissue, and 45% for human abdominal aorta tissue, have all been reported [151], [152]. Imaging in water to maintain a hydrated state caused attenuation of the low energy X-rays which would otherwise interact with the collagen, reducing contrast, and in some cases completely prevented the visualization of the gold-collagen scaffold (data not shown), suggesting a heterogeneous gold NP distribution throughout the collagen even at the level of the micro-CT. As the purpose of micro-CT was to assess the scaffold pore structure and not the gold nanoparticle distribution, a gold-collagen scaffold was stained with osmium tetroxide to enhance the collagen visualization of the scaffold while wet imaging. The mean 2D pore size of the critically point dried gold-collagen scaffold was 30% smaller than the hydrated gold-collagen scaffold, consistent with previously observed shrinkage of critically point dried tissues. Additionally, a study of a collagen scaffold showed shrinkage from 50-80% after critical point drying depending on the collagen dispersion (% weight/volume ratio) in the scaffold, with higher collagen dispersions having lower shrinkage [153], highlighting the importance of imaging the gold-collagen scaffold in a hydrated condition.

Comparing the 2D pore sizes of the dry gold-collagen scaffold with the 3D segmented pores, showed a lower pore size distribution for the 3D pores, although a higher pore size in 3D was expected because the possibility of measuring 2D pore diameters away from the centroid exists. The difference likely lies in the additional image processing steps that were taken to segment the pores prior to volume rendering. A morphological opening operation was performed to remove noise and assist the watershed separation. The effect of opening reduced the size of the pores while improving the boundaries between them. The ability of the watershed separation to identify and separate overlapping pores is dependant on a user controlled parameter that can influence the number of separated objects, and was adjusted through trial and error until accurate pore separation appeared to be achieved. It is possible that pore size reduction by opening, and segmentation of a true pore occurred, creating 3D

pores with artificially smaller volumes. Pore segmentation through morphological operations and watershed separation has been used prior to visualize pores of scaffold in 3D [154], [155], and is a suggested method by the Avizo software used in this work [148]. This discrepancy between the pore sizes measured in 2D and 3D with the same data set demonstrates the need for improved methods or standardized protocols for accurate pore structure assessment that do not rely on user interpretation and parameter selection.

The porosity and pore size of 3D scaffolds have direct implications on their functionality during biomedical applications. Open porous networks are important for cell nutrition, proliferation, and migration, and for tissue vascularization and formation. The porosity and mean pore size of scaffolds has been shown to significantly influence cell adhesion, viability and functionality, and depends on the cell type [156]. Although, trends exist showing cellular adhesion decreases with increasing pore size, while cellular aggregation, proliferation and differentiation increases with pore size and porosity for collagen based scaffolds [157], [158]. In general, tissue scaffolds with porosity greater than 50% and pore sizes larger than 100 μm can facilitate cellular function and tissue regeneration [156].

Transmission electron microscopy enabled high resolution visualization of the gold NPs functionalized on the collagen scaffold, revealing a homogeneous single NP size distribution, but a heterogeneous agglomerate size distribution, and gold spatial distribution, within the sampled sections. It is important to understand how the gold NPs are distributed throughout the collagen because it is the gold which represents the presence of collagen within contrast enhanced X-ray tomography images. The size of the individual gold NPs were consistent with gold NPs synthesized using the Turkevich method [146], however a wide range of NP agglomerates were identified. Although the gold NPs are non-uniformly distributed throughout the collagen scaffold at the nanoscale, providing insight on the resultant structure of the gold distribution as a function of the fabrication method, the impact of the gold NP spatial distribution on collagen detection in X-ray CT images is dependant on the resolution of the scanner during acquisition. *In vivo* and clinical CT scanners have voxel resolutions typically around 10 and 100 μm, respectively [132], [159], at which the dispersion of the gold within the collagen would appear uniform and reduce the impact of nanoscale distribution.

In addition to their ability to improve contrast for imaging, gold NPs have been used to functionalize collagen scaffolds due to their unique properties including: enhanced mechanical stability, resistance against enzymatic degradation, enhanced biocompatibility, anti-inflammatory, and antimicrobial properties [160]–[162]. In these studies the distribution of the gold NPs throughout the scaffolds was not of interest, however, investigation of gold NP attachment was performed using SEM and TEM in two of the three examples [160], [162].

Other studies such as those investigating catalyst NPs have used TEM [163], STEM [164] or ET [165] to determine the NP size, or spatial distribution [166]. In all cases the exact method of measurement to quantify the size and spatial distributions was either not specified, performed manually, or automated after image processing. Image processing steps also tend not be described. Manual measurement of NPs is a time-consuming process, and is limited by the ability of the investigator to accurately perform the measurement. Whereas automatic

measurements are prone to artificial alterations of the image, which is also commonly user controlled. Assessing NP size in 3D is limited due to missing wedge artifacts which elongate the NPs, increasing the measured size. In addition to errors associated with measuring the size of NPs, TEM specimens are prone to spatial artifacts. Nanoparticle clustering can occur after dehydration and embedding due to volume reduction, and when ultramicrotomes are used to make the sections, the knife can pull and distort NPs (although this is unlikely for our gold-collagen scaffolds as size of the NPs is smaller than the cut sections).

Assuming a negligible effect of the sample preparation process on the NP distribution, the observed trends are likely to be the result of certain processing steps during scaffold fabrication, such as centrifugation and compression.

Conclusion

A gold functionalized collagen scaffold for tissue engineering applications has been developed using a compression loading and poragen leaching process. This scaffold design is intended for improved detection of scaffold degradation behaviour *in vivo* using X-ray CT. The resultant scaffold structure after fabrication is of importance for predicting and understanding the outcomes of *in vivo* experiments.

Micro-CT revealed a highly porous and interconnected structure, with conflicting 2D and 3D pore sizes measurements. The 2D pore size was significantly larger when the scaffold was imaged in wet conditions, highlighting the importance of maintaining a hydrated state when imaging tissue scaffolds, but results in reduced contrast that requires additional staining or image processing steps. The pore structure investigated by micro-CT suggests the gold-collagen scaffold would be sufficient to facilitate cellular function and tissue regeneration.

TEM revealed a homogeneous gold NP size distribution, and heterogeneous agglomerate size and spatial distribution throughout the collagen. The majority of NPs were individually dispersed; however, a large range of NP agglomerates were noted. While this nanoscale non-uniform dispersion can limit the accuracy of *in vivo* studies using nanometer resolution CT techniques (e.g. synchrotron source CT), with the current resolving power of *in vivo* and clinical X-ray CT, the NPs are likely to be sufficiently dispersed.

The complementary nature of micro-CT and TEM allowed the structure of a gold functionalized collagen scaffold to be characterized in 3D, non-destructively, and with high resolution. Continued development of an appropriate protocol for imaging the hydrated gold-collagen scaffold in 3D, both by micro-CT and TEM would improve assessment of the true scaffold pore structure and NP distribution. Additional studies to improve the assessment of the gold NP distribution through the entire scaffold volume would also be advantageous. Overall, these techniques are a promising approach to guide the iterative development of new collagen scaffold materials.

CHAPTER 4: SUMMARY OF FINDINGS AND OVERALL CONCLUSIONS

The research presented in this thesis included the study of two diverse biomaterials: a titanium dental implant, and a collagen tissue scaffold. Although the goals of each study were different, they both required the investigation of 3D structural or functional properties at multiple length scales from the micrometer to the nanometer scale. X-ray and electron microscopy were selected as appropriate characterization tools that were optimized and applied for each study.

In both studies, micro-CT provided relatively non-destructive 3D visualization of the biomaterials with resolutions less than 5μm. This enabled new bone growth around and down the SIT dental implant to be accurately investigated. In the case of the gold-collagen scaffold, micro-CT enabled the complete assessment of the scaffold pore structure, a highly interconnected 3D organization. However, limitations did occur. When imaging the SIT implant, the contrast of the bone was reduced due to the presence of the relatively high X-ray attenuation of the metallic implants, demonstrating the challenge when imaging two different materials simultaneously with micro-CT. This limited our ability to differentiate new bone from old bone, which is otherwise identifiable by contrast gradients. In addition, beam hardening at the SIT implants caused streaking artifacts, reducing the identification of bone in contact. Contrast limitations also occurred when imaging the collagen scaffold, especially in water, which attenuated many of the low energy X-rays before reaching the scaffold. Limitations associated with contrast highlight the need for proper and uniform contrast enhancement.

SEM and TEM were used to investigate features of the SIT implant and collagen scaffold which were within the nanometer length scale. The bone-implant interface of the SIT implant was easily observed and assessed using SEM. TEM demonstrated its resolving power by effectively imaging the collagen fibril structure of the new bone neighbouring the SIT implant, displaying the process of bone remodelling and maturation. In addition, TEM demonstrated the spatial distribution, and extent of agglomeration of the gold NPs functionalized to the collagen scaffold. Although few artifacts were observed due to the imaging mechanism itself, artifacts related to the preparation of samples were present, particularly for the bone-implant samples. Separations of the implant-bone interface due to sample preparation were observed, indicated by a congruent curvature of the bone and neighbouring implant. Tissue collapse during dehydration, mechanical separation during low speed sawing, and exaggerated milling during *in situ* lift out, all have the potential to artificially separate the bone-implant interface before imaging, demonstrating the importance of careful sample preparation and the need to develop methods that reduce sample preparation requirements. A significant limitation of the TEM which impacted the gold NP findings, is the small sampling of the scaffold volume used to describe the NPs distribution throughout its entire volume. As resolving power improves, the employed magnification tends to increase, leading to even smaller spatial sampling. Developments in technology or methods to investigate large volumes of materials with high resolution, but maintaining an appropriate volume assessment is crucial for the field of microscopy.

In conclusion, X-ray and electron microscopy was successfully utilized to investigate the structure and function of two diverse biomaterials, demonstrating their complementary ability to work together, and in conjunction with other methods, for the study of a broad class of biomaterials.

REFERENCES

[1] J. Irish, "A 5,500-year old artifical human tooth from Egypt: a historical note," *J. Archaeol. Sci.*, vol. 19, no. 5, pp. 645–647, 2004.

[2] G. Seguin, E. d'Incau, P. Murail, and B. Maureille, "The earliest dental prosthesis in Celtic Gaul? The case of an Iron Age burial at Le Chêne, France," *Antiquity*, vol. 88, no. 340, pp. 488–500, 2014.

[3] L. Gaviria, J. P. Salcido, T. Guda, and J. L. Ong, "Current trends in dental implants.," *J. Korean Assoc. Oral Maxillofac. Surg.*, vol. 40, no. 2, pp. 50–60, 2014.

[4] D. Pitt and J.-M. Aubin, "Joseph Lister: father of modern surgery.," *Can. J. Surg.*, vol. 55, no. 5, pp. E8-9, Oct. 2012.

[5] J. Bartoníček, "Early history of operative treatment of fractures," *Arch. Orthop. Trauma Surg.*, vol. 130, no. 11, pp. 1385–1396, 2010.

[6] J. B. Park and R. S. Lakes, *Biomaterials : an introduction*. Springer, 2007.

[7] B. D. Ratner, *Biomaterials science : an introduction to materials in medicine*. Elsevier Academic Press, 2004.

[8] R. S. Greco, F. B. Prinz, and R. L. (Robert L. Smith, *Nanoscale technology in biological systems*. CRC Press, 2005.

[9] "Clinical Applications of Biomaterials," *NIH Consens Statement*, vol. 4, no. 5, p. 4(5):1-19, 1982.

[10] D. F. Williams, *Definitions in biomaterials : proceedings of a consensus conference of the European Society for Biomaterials, Chester, England, March 3-5, 1986*. Elsevier, 1987.

[11] D. F. Williams, *The Williams dictionary of biomaterials*. Liverpool University Press, 1999.

[12] J. P. Fisher, Ed., *Tissue Engineering*, vol. 585. Boston, MA: Springer US, 2007.

[13] H. Ma *et al.*, "3D printing of biomaterials with mussel-inspired nanostructures for tumor therapy and tissue regeneration," *Biomaterials*, vol. 111, pp. 138–148, Dec. 2016.

[14] L. Shor *et al.*, "Precision extruding deposition (PED) fabrication of polycaprolactone (PCL) scaffolds for bone tissue engineering," *Biofabrication*, vol. 1, no. 1, p. 15003, Mar. 2009.

[15] J. Y. Lee, C. A. Bashur, A. S. Goldstein, and C. E. Schmidt, "Polypyrrole-coated electrospun PLGA nanofibers for neural tissue applications," *Biomaterials*, vol. 30, no. 26, pp. 4325–4335, Sep. 2009.

[16] S. J. Hollister, "Porous scaffold design for tissue engineering," *Nat. Mater.*, vol. 4, no. 7, pp. 518–524, Jul. 2005.

[17] Q. Chen and G. A. Thouas, "Metallic implant biomaterials," *Mater. Sci. Eng. R Reports*, vol. 87, pp. 1–57, 2015.

[18] M. Niinomi, "Metallic biomaterials," *J. Artif. Organs*, vol. 11, no. 3, pp. 105–110, Sep. 2008.

[19] A. A. Appel, M. A. Anastasio, J. C. Larson, and E. M. Brey, "Imaging challenges in biomaterials and tissue engineering," *Biomaterials*, vol. 34, no. 28, pp. 6615–6630, Sep. 2013.

[20] A. Elliott, "Medical imaging," *Nucl. Instruments Methods Phys. Res. Sect. A Accel. Spectrometers, Detect. Assoc. Equip.*, vol. 546, no. 1–2, pp. 1–13, Jul. 2005.

[21] R. Mizutani and Y. Suzuki, "X-ray microtomography in biology," *Micron*, vol. 43, no. 2–3, pp. 104–115, Feb. 2012.

[22] R. Cierniak, *X-Ray Computed Tomography in Biomedical Engineering*. London: Springer London, 2011.

[23] R. Zhou *et al.*, "Study of the Microfocus X-Ray Tube Based on a Point-Like Target Used for Micro-Computed Tomography," *PLoS One*, vol. 11, no. 6, p. e0156224, Jun. 2016.

[24] J.-T. Hsu, Y.-W. Shen, C.-W. Kuo, R.-T. Wang, L.-J. Fuh, and H.-L. Huang, "Impacts of 3D bone-to- implant contact and implant diameter on primary stability of dental implant," *J. Formos. Med. Assoc.*, May 2017.

[25] S. Vandeweghe, P. G. Coelho, C. Vanhove, A. Wennerberg, and R. Jimbo, "Utilizing micro-computed tomography to evaluate bone structure surrounding dental implants: A comparison with histomorphometry," *J. Biomed. Mater. Res. - Part B Appl. Biomater.*, vol. 101, no. 7, pp. 1259–1266, 2013.

[26] B. Sagbas and M. Numan Durakbasa, "Measurement of Wear in Orthopedic Prosthesis," *Acta Phys. Pol. A*, vol. 121, no. 1, pp. 131–134, Jan. 2012.

[27] S. Affatato, F. Zanini, and S. Carmignato, "Micro X-Ray Computed Tomography Mass Loss Assessment of Different UHMWPE: A Hip Joint Simulator Study on Standard vs. Cross-Linked Polyethylene.," *PLoS One*, vol. 12, no. 1, p. e0170263, 2017.

[28] A. Jedenmalm *et al.*, "Validation of a 3D CT method for measurement of linear wear of acetabular cups.," *Acta Orthop.*, vol. 82, no. 1, pp. 35–41, Feb. 2011.

[29] O. Atali *et al.*, "Bone healing after biodegradable mini-plate fixation," *Acta Cir. Bras.*, vol. 31, no. 6, pp. 364–370, Jun. 2016.

[30] R. Steck *et al.*, "Influence of internal fixator flexibility on murine fracture healing as characterized by mechanical testing and microCT imaging," *J. Orthop. Res.*, vol. 29, no. 8, pp. 1245–1250, Aug. 2011.

[31] M. Plecko *et al.*, "Osseointegration and biocompatibility of different metal implants-

-a comparative experimental investigation in sheep.," *BMC Musculoskelet. Disord.*, vol. 13, p. 32, Mar. 2012.

[32] M. Geetha, a. K. Singh, R. Asokamani, and a. K. Gogia, "Ti based biomaterials, the ultimate choice for orthopaedic implants – A review," *Prog. Mater. Sci.*, vol. 54, no. 3, pp. 397–425, May 2009.

[33] S. Furqan *et al.*, "The use of x-ray micro-computed tomography for evaluation of bone growth in 3D printed metal implants - Correlation with histology," *Front. Bioeng. Biotechnol.*, vol. 4, 2016.

[34] A. Palmquist, A. Snis, L. Emanuelsson, M. Browne, and P. Thomsen, "Long-term biocompatibility and osseointegration of electron beam melted, free-form-fabricated solid and porous titanium alloy: Experimental studies in sheep," *J. Biomater. Appl.*, vol. 0, no. 0, pp. 1–14, 2011.

[35] E. Baril, L. P. Lefebvre, and S. A. Hacking, "Direct visualization and quantification of bone growth into porous titanium implants using micro computed tomography," *J. Mater. Sci. Mater. Med.*, vol. 22, no. 5, pp. 1321–1332, May 2011.

[36] R. Schulze *et al.*, "Artefacts in CBCT: a review.," *Dentomaxillofac. Radiol.*, vol. 40, no. 5, pp. 265–73, Jul. 2011.

[37] R. K. W. Schulze, D. Berndt, and B. D'Hoedt, "On cone-beam computed tomography artifacts induced by titanium implants," *Clin. Oral Implants Res.*, vol. 21, no. 1, pp. 100–107, Jan. 2010.

[38] H. Sarve, J. Lindblad, G. Borgefors, and C. B. Johansson, "Extracting 3D information on bone remodeling in the proximity of titanium implants in SR micro-CT image volumes," *Comput. Methods Programs Biomed.*, vol. 102, no. 1, pp. 25–34, 2011.

[39] J. A. Meganck, K. M. Kozloff, M. M. Thornton, S. M. Broski, and S. A. Goldstein, "Beam hardening artifacts in micro-computed tomography scanning can be reduced by X-ray beam filtration and the resulting images can be used to accurately measure BMD.," *Bone*, vol. 45, no. 6, pp. 1104–16, Dec. 2009.

[40] Lopes, Costa, and de Jesus EF, "Computed tomography with monochromatic bremsstrahlung radiation," *Appl. Radiat. Isot.*, vol. 53, no. 4–5, pp. 665–71, Oct. 2000.

[41] J. M. Verburg and J. Seco, "CT metal artifact reduction method correcting for beam hardening and missing projections," *Phys. Med. Biol.*, vol. 57, no. 9, pp. 2803–2818, May 2012.

[42] J. Zidek *et al.*, "Accurate micro-computed tomography imaging of pore spaces in collagen-based scaffold," *J. Mater. Sci. Mater. Med.*, vol. 27, no. 6, p. 110, Jun. 2016.

[43] M. J. Moore *et al.*, "Quantitative analysis of interconnectivity of porous

biodegradable scaffolds with micro-computed tomography," *J. Biomed. Mater. Res.*, vol. 71A, no. 2, pp. 258–267, Nov. 2004.

[44] S. Bertoldi, S. Farè, and M. C. Tanzi, "Assessment of scaffold porosity: the new route of micro-CT," *J. Appl. Biomater. Biomech.*, vol. 9, no. 3, pp. 165–175, 2011.

[45] F. J. O'Brien, "Biomaterials & scaffolds for tissue engineering," *Mater. Today*, vol. 14, no. 3, pp. 88–95, Mar. 2011.

[46] S. Y. Nam, L. M. Ricles, L. J. Suggs, and S. Y. Emelianov, "Imaging strategies for tissue engineering applications.," *Tissue Eng. Part B. Rev.*, vol. 21, no. 1, pp. 88–102, Feb. 2015.

[47] H. Lusic and M. W. Grinstaff, "X-ray-computed tomography contrast agents.," *Chem. Rev.*, vol. 113, no. 3, pp. 1641–66, Mar. 2013.

[48] D. Kim, S. Park, J. H. Lee, Y. Y. Jeong, and Sangyong Jon, "Antibiofouling Polymer-Coated Gold Nanoparticles as a Contrast Agent for in Vivo X-ray Computed Tomography Imaging," 2007.

[49] S. M. Forton *et al.*, "*In Vivo* Microcomputed Tomography of Nanocrystal-Doped Tissue Engineered Scaffolds," *ACS Biomater. Sci. Eng.*, vol. 2, no. 4, pp. 508–516, Apr. 2016.

[50] K. A. Faraj *et al.*, "Micro-Computed Tomographical Imaging of Soft Biological Materials Using Contrast Techniques," *Tissue Eng. Part C Methods*, vol. 15, no. 3, pp. 493–499, Sep. 2009.

[51] S. Wischnitzer, *Introduction to electron microscopy*, 3d ed.--. Pergamon Press, 1981.

[52] D. B. Williams and C. B. Carter, *Transmission Electron Microscopy*. Boston, MA: Springer US, 2009.

[53] M. Vielreicher *et al.*, "Taking a deep look: modern microscopy technologies to optimize the design and functionality of biocompatible scaffolds for tissue engineering in regenerative medicine.," *J. R. Soc. Interface*, vol. 10, no. 86, p. 20130263, Sep. 2013.

[54] S. A. Hacking *et al.*, "Surface roughness enhances the osseointegration of titanium headposts in non-human primates," *J. Neurosci. Methods*, vol. 211, no. 2, pp. 237–244, Nov. 2012.

[55] A. Barfeie, J. Wilson, and J. Rees, "Implant surface characteristics and their effect on osseointegration," *BDJ*, vol. 218, no. 5, pp. E9–E9, Mar. 2015.

[56] R. K. Alla, K. Ginjupalli, N. Upadhya, M. Shammas, R. K. Ravi, and R. Sekhar, "Surface Roughness of Implants: A Review," *Trends Biomater. Artif. Organs*, vol. 25, no. 3, pp. 112–118, 2011.

[57] R. Brånemark, L. Emanuelsson, A. Palmquist, and P. Thomsen, "Bone response to laser-induced micro- and nano-size titanium surface features," *Nanomedicine*

Nanotechnology, Biol. Med., vol. 7, no. 2, pp. 220–227, 2011.

[58] A. Palmquist, L. Emanuelsson, R. Brånemark, and P. Thomsen, "Biomechanical, histological and ultrastructural analyses of laser micro- and nano-structured titanium implant after 6 months in rabbit," *J. Biomed. Mater. Res. Part B Appl. Biomater.*, vol. 97B, no. 2, pp. 289–298, May 2011.

[59] P. Pachauri, L. R. Bathala, and R. Sangur, "Techniques for dental implant nanosurface modifications.," *J. Adv. Prosthodont.*, vol. 6, no. 6, pp. 498–504, Dec. 2014.

[60] N. M. Poulos *et al.*, "Evaluation of a novel calcium phosphate-coated titanium porous oxide implant surface: a study in rabbits.," *Int. J. Oral Maxillofac. Implants*, vol. 26, no. 4, pp. 731–738, 2011.

[61] K. Grandfield, S. Pujari, M. Ott, H. Engqvist, and W. Xia, "Effect of Calcium and Strontium on Mesoporous Titania Coatings for Implant Applications," *J. Biomater. Nanobiotechnol.*, vol. 4, pp. 107–113, 2013.

[62] R. Junker, A. Dimakis, M. Thoneick, and J. A. Jansen, "Effects of implant surface coatings and composition on bone integration: a systematic review," *Clin. Oral Implants Res.*, vol. 20, pp. 185–206, Sep. 2009.

[63] C. Mangano *et al.*, "Scanning electron microscopy (SEM) and X-ray dispersive spectrometry evaluation of direct laser metal sintering surface and human bone interface: A case series," *Lasers Med. Sci.*, vol. 26, no. 1, pp. 133–138, 2011.

[64] N. El-Mekawy, M. M. Fouad, Y. M. El-Hawary, M. A. Al-Shahat, and R. El-Gendy, "Scanning Electron Microscopy Observations of Osseointegration Failures of Dental Implants that Support Mandibular Overdentures," *Implant Dent.*, vol. 22, no. 6, pp. 645–649, Dec. 2013.

[65] K. Grandfield *et al.*, "Ultrastructural characterisation of the hydroxyapatite-coated pedicle screw and human bone interface," *Int. J. Nano Biomater.*, vol. 4, no. 1, p. 1, 2012.

[66] J.-S. Kim *et al.*, "Nanoscale Bonding between Human Bone and Titanium Surfaces: Osseohybridization," *Biomed Res. Int.*, vol. 2015, pp. 1–10, Jan. 2015.

[67] X. Wang, F. A. Shah, A. Palmquist, and K. Grandfield, "3D Characterization of Human Nano-osseointegration by On-Axis Electron Tomography without the Missing Wedge," *ACS Biomater. Sci. Eng.*, vol. 3, no. 1, pp. 49–55, Jan. 2017.

[68] M. M. Erol *et al.*, "Copper-releasing, boron-containing bioactive glass-based scaffolds coated with alginate for bone tissue engineering," *Acta Biomater.*, vol. 8, no. 2, pp. 792–801, Feb. 2012.

[69] A. Polini, D. Pisignano, M. Parodi, R. Quarto, and S. Scaglione, "Osteoinduction of Human Mesenchymal Stem Cells by Bioactive Composite Scaffolds without Supplemental Osteogenic Growth Factors," *PLoS One*, vol. 6, no. 10, p. e26211,

Oct. 2011.

[70] M. Vedhanayagam *et al.*, "Role of nanoparticle size in self-assemble processes of collagen for tissue engineering application," *Int. J. Biol. Macromol.*, vol. 99, pp. 655–664, Jun. 2017.

[71] L.-H. Li *et al.*, "Improved biological performance of Ti implants due to surface modification by micro-arc oxidation," *Biomaterials*, vol. 25, no. 14, pp. 2867–2875, 2004.

[72] S. Y. Madani, A. Tan, M. Dwek, and A. M. Seifalian, "Functionalization of single-walled carbon nanotubes and their binding to cancer cells.," *Int. J. Nanomedicine*, vol. 7, pp. 905–14, 2012.

[73] P. I. Brånemark *et al.*, "Osseointegrated implants in the treatment of the edentulous jaw. Experience from a 10-year period.," *Scand. J. Plast. Reconstr. Surg. Suppl.*, vol. 16, pp. 1–132, 1977.

[74] D. Tran, I. Gay, J. Diaz-Rodriguez, K. Parthasarathy, R. Weltman, and L. Friedman, "Survival of Dental Implants Placed in Grafted and Nongrafted Bone: A Retrospective Study in a University Setting No Title," *Int. J. Oral Maxillofac. Implant.*, vol. 31, no. 2, pp. 310–317, 2016.

[75] C. A. A. Lemos, M. L. F. Alves, R. Okamoto, M. R. Mendonça, and E. P. Pellizzer, "Short dental implants versus standard dental implants placed in the posterior jaws: A systematic review and meta-analysis," *J. Dent.*, vol. 47, pp. 8–17, 2016.

[76] H.-J. Han, S. Kim, and D.-H. Han, "Multifactorial evaluation of implant failure: a 19-year retrospective study.," *Int. J. Oral Maxillofac. Implants*, vol. 29, no. 2, pp. 303–10, 2014.

[77] H. L. Sun, C. Huang, Y. R. Wu, and B. Shi, "Failure Rates of Short ($\lesssim$ 10 mm) Dental Implants and Factors Influencing Their Failure: A Systematic Review.," *Int. J. Oral Maxillofac. Implants*, vol. 26, no. 4, pp. 816–825, 2011.

[78] S. Elangovan and V. Allareddy, "Estimates of Hospital Based Emergency Department Visits due to Dental Implant Failures in the United States," *J. Evid. Based Dent. Pract.*, vol. 16, no. 2, pp. 81–85, 2016.

[79] L. Carlsson, T. Rostlund, T. Albrektsson, B. Albrektsson, and P. Branemark, "Osseointegration of titanium implants," *Acta Odontol. Scand.*, vol. 57, no. 4, pp. 285–289, 1986.

[80] C. Oldani and A. Dominguez, "Titanium as a Biomaterial for Implants," in *Recent Advances in Athroplasty*, S. K. Fokter, Ed. InTech, 2012, pp. 149–162.

[81] B. E. J. Lee, S. Ho, G. Mestres, M. Karlsson Ott, P. Koshy, and K. Grandfield, "Dual-topography electrical discharge machining of titanium to improve biocompatibility," *Surf. Coatings Technol.*, vol. 296, pp. 149–156, 2016.

[82] F. A. Shah, X. Wang, P. Thomsen, K. Grandfield, and A. Palmquist, "High-Resolution Visualization of the Osteocyte Lacuno-Canalicular Network Juxtaposed to the Surface of Nanotextured Titanium Implants in Human," *ACS Biomater. Sci. Eng.*, vol. 1, no. 5, pp. 305–313, May 2015.

[83] A. Palmquist, L. Emanuelsson, R. Brãnemark, and P. Thomsen, "Biomechanical, histological and ultrastructural analyses of laser micro- and nano-structured titanium implant after 6 months in rabbit," *J. Biomed. Mater. Res. - Part B Appl. Biomater.*, vol. 97 B, no. 2, pp. 289–298, 2011.

[84] Y. T. Sul, J. Jönsson, G. S. Yoon, and C. Johansson, "Resonance frequency measurements in vivo and related surface properties of magnesium-incorporated, micropatterned and magnesium-incorporated TiUnite ®, Osseotite®, SLA® and TiOblast® implants," *Clin. Oral Implants Res.*, vol. 20, no. 10, pp. 1146–1155, 2009.

[85] O. E. Ogle, "Implant Surface Material, Design, and Osseointegration," *Dent. Clin. North Am.*, vol. 59, no. 2, pp. 505–520, 2015.

[86] T. B. Kim, S. Yue, Z. Zhang, E. Jones, J. R. Jones, and P. D. Lee, "Additive manufactured porous titanium structures: Through-process quantification of pore and strut networks," *J. Mater. Process. Technol.*, vol. 214, no. 11, pp. 2706–2715, 2014.

[87] J. Lv *et al.*, "Electron Beam Melting Fabrication of Porous Ti6Al4V Scaffolds: Cytocompatibility and Osteogenesis," *Adv. Eng. Mater.*, vol. 17, no. 9, pp. 1391–1398, Sep. 2015.

[88] F. A. Shah, A. Snis, A. Matic, P. Thomsen, and A. Palmquist, "3D printed Ti6Al4V implant surface promotes bone maturation and retains a higher density of less aged osteocytes at the bone-implant interface," *Acta Biomater.*, vol. 30, pp. 357–367, Jan. 2016.

[89] A. Cheng, A. Humayun, D. J. Cohen, B. D. Boyan, and Z. Schwartz, "Additively manufactured 3D porous Ti-6Al-4V constructs mimic trabecular bone structure and regulate osteoblast proliferation, differentiation and local factor production in a porosity and surface roughness dependent manner," *Biofabrication*, vol. 6, no. 4, p. 45007, Oct. 2014.

[90] J. S. Khurana, *Bone Structure, Development and Bone Biology*. 2009.

[91] J. S. Khurana, E. F. McCarthy, and P. J. Zhang, *Essentials in Bone and Soft-Tissue Pathology*. New York: Springer, 2009.

[92] S. L. Croker, W. Reed, and D. Donlon, "Comparative cortical bone thickness between the long bones of humans and five common non-human mammal taxa," *Forensic Sci. Int.*, vol. 260, p. 104.e1-104.e17, Mar. 2016.

[93] S. L. Croker, J. G. Clement, and D. Donlon, "A comparison of cortical bone thickness in the femoral midshaft of humans and two non-human mammals," *HOMO*

- *J. Comp. Hum. Biol.*, vol. 60, no. 6, pp. 551–565, Nov. 2009.

[94] M. Sadat-Ali, E. Elshaboury, A. S. Al-Omran, M. Q. Azam, A. Syed, and A. H. Gullenpet, "Tibial cortical thickness: A dependable tool for assessing osteoporosis in the absence of dual energy X-ray absorptiopmetry.," *Int. J. Appl. basic Med. Res.*, vol. 5, no. 1, pp. 21–4, 2015.

[95] E. M. Lillie, J. E. Urban, S. K. Lynch, A. A. Weaver, and J. D. Stitzel, "Evaluation of Skull Cortical Thickness Changes With Age and Sex From Computed Tomography Scans," *J. Bone Miner. Res.*, vol. 31, no. 2, pp. 299–307, Feb. 2016.

[96] D. Fernandes, C. Elias, and A. Ruellas, "Influence of Screw Length and Bone Thickness on the Stability of Temporary Implants," *Materials (Basel).*, vol. 8, no. 9, pp. 6558–6569, Sep. 2015.

[97] V. J. Cvetkovic *et al.*, "A comparison of the microarchitecture of lower limb long bones between some animal models and humans: a review," *Vet. Med. (Praha).*, vol. 58, no. 7, pp. 339–351, 2013.

[98] K. E. KADLER, D. F. HOLMES, J. A. TROTTER, and J. A. CHAPMAN, "Collagen fibril formation," *Biochem. J.*, vol. 316, no. 1, 1996.

[99] W. J. Landis, K. J. Hodgens, J. Arena, M. J. Song, and B. F. McEwen, "Structural relations between collagen and mineral in bone as determined by high voltage electron microscopic tomography," *Microsc. Res. Tech.*, vol. 33, no. 2, pp. 192–202, Feb. 1996.

[100] B. Alexander *et al.*, "The nanometre-scale physiology of bone: steric modelling and scanning transmission electron microscopy of collagen-mineral structure," *J. R. Soc. Interface*, vol. 9, no. 73, pp. 1774–1786, Aug. 2012.

[101] H. P. Schwarcz, "The ultrastructure of bone as revealed in electron microscopy of ion-milled sections," *Semin. Cell Dev. Biol.*, vol. 46, pp. 44–50, Oct. 2015.

[102] A. Scarano, G. A. Favero, E. Fiera, and A. Piattelli, "Histological Analysis of Soft-Tissues Biomaterial Interface," in *Handbook of Histology Methods for Bone and Cartilage*, Totowa, NJ: Humana Press, 2003, pp. 439–445.

[103] A. L. Mescher, *Junqueira's basic histology : text and atlas*, 14th ed. New York, NY: McGraw-Hill.

[104] M. H. Ross and W. Pawlina, *Histology : a text and atlas : with correlated cell and molecular biology*, 6th ed. Lippincott Williams & Wilkins, 2011.

[105] J. L. Ong and L. C. Lucas, "Auger electron spectroscopy and its use for the characterization of titanium and hydroxyapatite surfaces," *Biomaterials*, vol. 19, no. 4–5, pp. 455–464, Mar. 1998.

[106] J. C. Vickerman, "Secondary ion mass spectrometry-basic concepts, instrumental aspects, applications and trends. A. BENNINGHOVEN, F. G. RUDENAUER and

H. W. WERNER, Wiley, New York, 1987, 1277 pages," *Surf. Interface Anal.*, vol. 10, no. 8, pp. 435–435, Oct. 1987.

[107] K. Donath and G. Breuner, "A method for the study of undecalcified bones and teeth with attached soft tissues. The Säge-Schliff (sawing and grinding) technique.," *J. Oral Pathol.*, vol. 11, no. 4, pp. 318–326, 1982.

[108] L. A. Feldkamp, L. C. Davis, and J. W. Kress, "Practical cone-beam algorithm," *J. Opt. Soc. Am. A*, vol. 1, no. 6, p. 612, Jun. 1984.

[109] I. Yadroitsev and I. Smurov, "Surface Morphology in Selective Laser Melting of Metal Powders," *Phys. Procedia*, vol. 12, pp. 264–270, 2011.

[110] J. Pouilleau, D. Devilliers, F. Garrido, S. Durand-Vidal, and E. Mahé, "Structure and composition of passive titanium oxide films," *Mater. Sci. Eng. B*, vol. 47, no. 3, pp. 235–243, Jun. 1997.

[111] M. . Casaletto, G. . Ingo, S. Kaciulis, G. Mattogno, L. Pandolfi, and G. Scavia, "Surface studies of in vitro biocompatibility of titanium oxide coatings," *Appl. Surf. Sci.*, vol. 172, no. 1–2, pp. 167–177, Mar. 2001.

[112] X. W. Tan *et al.*, "In vivo evaluation of titanium oxide and hydroxyapatite as an artificial cornea skirt," *J. Mater. Sci. Mater. Med.*, vol. 23, no. 4, pp. 1063–1072, Apr. 2012.

[113] A. Palmquist, K. Grandfield, and B. Norlindh, "Bone-titanium oxide interface in humans revealed by transmission electron microscopy and electron tomography.," *J. R. Soc. Interface*, vol. 9, no. 67, pp. 396–400, Feb. 2012.

[114] C. Mangano *et al.*, "Early human bone response to laser metal sintering surface topography: a histologic report.," *J. Oral Implantol.*, vol. 36, no. 2, pp. 91–96, 2010.

[115] S. Stübinger *et al.*, "Histological and biomechanical analysis of porous additive manufactured implants made by direct metal laser sintering: A pilot study in sheep," *J. Biomed. Mater. Res. - Part B Appl. Biomater.*, vol. 101, no. 7, pp. 1154–1163, 2013.

[116] M. Carlo *et al.*, "Histological and Synchrotron Radiation-Based Computed Microtomography Study of 2 Human-Retrieved Direct Laser Metal Formed Titanium Implants," *Implant Dent.*, vol. 0, no. 0, pp. 1–5, 2013.

[117] A. Piattelli, *Bone Response to Dental Implant Materials*. Woodhead Publishing, 2016.

[118] C. C. Villar, G. Huynh-Ba, M. P. Mills, and D. L. Cochran, "Wound healing around dental implants," *Endod. Top.*, vol. 25, no. 1, pp. 44–62, Sep. 2011.

[119] R. N. Brown *et al.*, "Comparison of stainless steel and titanium alloy orthodontic miniscrew implants: A mechanical and histologic analysis," *Am. J. Orthod. Dentofac. Orthop.*, vol. 145, no. 4, pp. 496–504, 2014.

[120] J. E. Davies, "Understanding peri-implant endosseous healing.," *J. Dent. Educ.*, vol. 67, no. 8, pp. 932–49, Aug. 2003.

[121] W. Chang *et al.*, "A newly designed resonance frequency analysis device for dental imlpant stability detection," *Dent. Mater. J.*, vol. 26, no. 5, pp. 665–671, 2007.

[122] C. Aparicio, A. Padrós, and F.-J. Gil, "In vivo evaluation of micro-rough and bioactive titanium dental implants using histometry and pull-out tests," *J. Mech. Behav. Biomed. Mater.*, vol. 4, no. 8, pp. 1672–1682, Nov. 2011.

[123] S. F. Alves and T. Wassall, "In vitro evaluation of osteoblastic cell adhesion on machined osseointegrated implants," *Braz. Oral Res.*, vol. 23, no. 2, pp. 131–136, Jun. 2009.

[124] G. Li *et al.*, "In vitro and in vivo study of additive manufactured porous Ti6Al4V scaffolds for repairing bone defects," *Sci. Rep.*, vol. 6, p. 34072, Sep. 2016.

[125] D. J. Cohen *et al.*, "Performance of laser sintered Ti–6Al–4V implants with bone-inspired porosity and micro/nanoscale surface roughness in the rabbit femur," *Biomed. Mater.*, vol. 12, no. 2, p. 25021, Apr. 2017.

[126] K. Gulati *et al.*, "Anodized 3D-printed titanium implants with dual micro- and nano-scale topography promote interaction with human osteoblasts and osteocyte-like cells," *J. Tissue Eng. Regen. Med.*, 2016.

[127] Y. Dang *et al.*, "In vivo osseointegration of Ti implants with a strontium-containing nanotubular coating.," *Int. J. Nanomedicine*, vol. 11, pp. 1003–11, 2016.

[128] X. Chen, X. C. Zhou, S. Liu, R. F. Wu, C. Aparicio, and J. Y. Wu, "In vivo osseointegration of dental implants with an antimicrobial peptide coating," *J. Mater. Sci. Mater. Med.*, vol. 28, no. 5, p. 76, May 2017.

[129] V. Sollazzo *et al.*, "Zirconium oxide coating improves implant osseointegration in vivo," *Dent. Mater.*, vol. 24, no. 3, pp. 357–361, Mar. 2008.

[130] B. W. Tillman *et al.*, "Bioengineered vascular access maintains structural integrity in response to arteriovenous flow and repeated needle puncture," *J. Vasc. Surg.*, vol. 56, no. 3, pp. 783–793, Sep. 2012.

[131] S. H. Kim *et al.*, "Near-Infrared Fluorescence Imaging for Noninvasive Trafficking of Scaffold Degradation," *Sci. Rep.*, vol. 3, p. 1198, Feb. 2013.

[132] Z. Starosolski *et al.*, "Ultra High-Resolution In vivo Computed Tomography Imaging of Mouse Cerebrovasculature Using a Long Circulating Blood Pool Contrast Agent," *Sci. Rep.*, vol. 5, no. 1, p. 10178, Sep. 2015.

[133] S. H. Yun and S. J. J. Kwok, "Light in diagnosis, therapy and surgery," *Nat. Biomed. Eng.*, vol. 1, no. 1, p. 8, Jan. 2017.

[134] A. Aisen, W. Martel, E. Braunstein, K. McMillin, W. Phillips, and T. Kling, "MRI and CT evaluation of primary bone and soft-tissue tumors," *Am. J. Roentgenol.*, vol.

146, no. 4, pp. 749–756, Apr. 1986.

[135] E. Gale Group., D. Van Loo, P. Cornillie, L. Brabant, and L. Van Hoorebeke, "An exploratory study of contrast agents for soft tissue visualization by means of high resolution X-ray computed tomography imaging," *J. Microsc.*, vol. 250, no. 1, pp. 21–31, 2013.

[136] S. Ahn, H. Yoon, G. Kim, Y. Kim, S. Lee, and W. Chun, "Designed Three-Dimensional Collagen Scaffolds for Skin Tissue Regeneration," *Tissue Eng. Part C Methods*, vol. 16, no. 5, pp. 813–820, Oct. 2010.

[137] S. M. Oliveira *et al.*, "An improved collagen scaffold for skeletal regeneration.," *J. Biomed. Mater. Res. A*, vol. 94, no. 2, pp. 371–9, Aug. 2010.

[138] S. Yoshii and M. Oka, "Collagen filaments as a scaffold for nerve regeneration.," *J. Biomed. Mater. Res.*, vol. 56, no. 3, pp. 400–5, Sep. 2001.

[139] L. E. Cole, R. D. Ross, J. M. Tilley, T. Vargo-Gogola, and R. K. Roeder, "Gold nanoparticles as contrast agents in x-ray imaging and computed tomography," *Nanomedicine*, vol. 10, no. 2, pp. 321–341, Jan. 2015.

[140] L. Paavolainen *et al.*, "Compensation of Missing Wedge Effects with Sequential Statistical Reconstruction in Electron Tomography," *PLoS One*, vol. 9, no. 10, p. e108978, Oct. 2014.

[141] M. Weyland and P. A. Midgley, "Electron tomography," *Mater. Today*, vol. 7, no. 12, pp. 32–40, Dec. 2004.

[142] H. Winkler and K. A. Taylor, "Accurate marker-free alignment with simultaneous geometry determination and reconstruction of tilt series in electron tomography," *Ultramicroscopy*, vol. 106, no. 3, pp. 240–254, Feb. 2006.

[143] M. Cao, A. Takaoka, H.-B. Zhang, and R. Nishi, "An automatic method of detecting and tracking fiducial markers for alignment in electron tomography," *J. Electron Microsc. (Tokyo).*, vol. 60, no. 1, pp. 39–46, Feb. 2011.

[144] L. Norlen, O. Oktem, and U. Skoglund, "Molecular cryo-electron tomography of vitreous tissue sections: current challenges," *J. Microsc.*, vol. 235, no. 3, pp. 293–307, Sep. 2009.

[145] R. J. Kane *et al.*, "Hydroxyapatite reinforced collagen scaffolds with improved architecture and mechanical properties," *Acta Biomater.*, vol. 17, pp. 16–25, Apr. 2015.

[146] J. Turkevich, P. C. Stevenson, and J. Hillier, "A Study of the nucleation and growth processes in the synthesis of colloidal gold," *Discuss. Faraday Soc.*, vol. 11, pp. 55–75, 1951.

[147] N. Reznikov, R. Almany-Magal, R. Shahar, and S. Weiner, "Three-dimensional imaging of collagen fibril organization in rat circumferential lamellar bone using a

dual beam electron microscope reveals ordered and disordered sub-lamellar structures," *Bone*, vol. 52, no. 2, pp. 676–683, Feb. 2013.

[148] FEI, "Avizo ® 9 User's Guide." FEI.

[149] E. S. Reynolds, "The use of lead citrate at high pH as an electron-opaque stain in electron microscopy.," *J. Cell Biol.*, vol. 17, no. 1, pp. 208–12, Apr. 1963.

[150] J. Arends and J. Ruben, "Effect of air-drying on demineralized and on sound coronal human dentine: a study on density and on lesion shrinkage.," *Caries Res.*, vol. 29, no. 1, pp. 14–9, 1995.

[151] M. V. King, "Dimensional changes in cells and tissues during specimen preparation for the electron microscope," *Cell Biophys.*, vol. 18, no. 1, pp. 31–55, Feb. 1991.

[152] A. Boyde and E. MacOnnachie, "Volume changes during preparation of mouse embryonic tissue for scanning electron microscopy," *Scanning*, vol. 2, no. 3, pp. 149–163, Jan. 1979.

[153] E. Sachlos, "Novel collagen scaffolds with predefined internal morphology made by solid freeform fabrication," *Biomaterials*, vol. 24, no. 8, pp. 1487–1497, Apr. 2003.

[154] J. R. Jones, R. C. Atwood, G. Poologasundarampillai, S. Yue, and P. D. Lee, "Quantifying the 3D macrostructure of tissue scaffolds," *J. Mater. Sci. Mater. Med.*, vol. 20, no. 2, pp. 463–471, Feb. 2009.

[155] J. R. Jones, G. Poologasundarampillai, R. C. Atwood, D. Bernard, and P. D. Lee, "Non-destructive quantitative 3D analysis for the optimisation of tissue scaffolds," *Biomaterials*, vol. 28, no. 7, pp. 1404–1413, Mar. 2007.

[156] Q. L. Loh and C. Choong, "Three-dimensional scaffolds for tissue engineering applications: role of porosity and pore size.," *Tissue Eng. Part B. Rev.*, vol. 19, no. 6, pp. 485–502, Dec. 2013.

[157] F. J. O'Brien, B. A. Harley, I. V. Yannas, and L. J. Gibson, "The effect of pore size on cell adhesion in collagen-GAG scaffolds," *Biomaterials*, vol. 26, no. 4, pp. 433–441, Feb. 2005.

[158] C. M. Murphy, M. G. Haugh, and F. J. O'Brien, "The effect of mean pore size on cell attachment, proliferation and migration in collagen–glycosaminoglycan scaffolds for bone tissue engineering," *Biomaterials*, vol. 31, no. 3, pp. 461–466, Jan. 2010.

[159] A. J. Burghardt, T. M. Link, and S. Majumdar, "High-resolution Computed Tomography for Clinical Imaging of Bone Microarchitecture," *Clin. Orthop. Relat. Res.*, vol. 469, no. 8, pp. 2179–2193, Aug. 2011.

[160] S. A. Grant *et al.*, "Assessment of the biocompatibility and stability of a gold nanoparticle collagen bioscaffold," *J. Biomed. Mater. Res. Part A*, vol. 102, no. 2, pp. 332–339, Feb. 2014.

[161] O. Akturk *et al.*, "Collagen/gold nanoparticle nanocomposites: A potential skin wound healing biomaterial," *J. Biomater. Appl.*, vol. 31, no. 2, pp. 283–301, Aug. 2016.

[162] C. R. Deeken, D. B. Fox, S. L. Bachman, B. J. Ramshaw, and S. A. Grant, "Characterization of bionanocomposite scaffolds comprised of amine-functionalized gold nanoparticles and silicon carbide nanowires crosslinked to an acellular porcine tendon," *J. Biomed. Mater. Res. Part B Appl. Biomater.*, vol. 97B, no. 2, pp. 334–344, May 2011.

[163] E. Terrado, I. Tacchini, A. M. Benito, W. K. Maser, and M. T. Martínez, "Optimizing catalyst nanoparticle distribution to produce densely-packed carbon nanotube growth," *Carbon N. Y.*, vol. 47, no. 8, pp. 1989–2001, Jul. 2009.

[164] T. Pingel, M. Skoglundh, H. Gronbeck, and E. Olsson, "Revealing local variations in nanoparticle size distributions in supported catalysts: a generic TEM specimen preparation method," *J. Microsc.*, vol. 260, no. 2, pp. 125–132, Nov. 2015.

[165] D. Rossouw, L. Chinchilla, N. Kremliakova, and G. A. Botton, "The 3D Nanoscale Evolution of Platinum-Niobium Oxide Fuel Cell Catalysts via Identical Location Electron Tomography," *Part. Part. Syst. Charact.*, vol. 34, no. 7, p. 1700051, Jul. 2017.

[166] G. Prieto, J. D. Meeldijk, K. P. de Jong, and P. E. de Jongh, "Interplay between pore size and nanoparticle spatial distribution: Consequences for the stability of CuZn/SiO2 methanol synthesis catalysts," *J. Catal.*, vol. 303, pp. 31–40, Jul. 2013.

[167] G. J. Tortora and B. Derrickson, *Principles of anatomy and physiology*. John Wiley & Sons, 2010.